A. Mannarino, P. Mantegazza
Multifidelity Control of Aeroelastic Systems: an Immersion and Invariance Approach
Journal of Guidance Control and Dynamics, Vol. 37, N. 5, 2014, p. 1568-1582
doi:10.2514/1.G000329

Multi-Fidelity Control of Aeroelastic Systems: An Immersion And Invariance Approach

Andrea Mannarino* and Paolo Mantegazza†

Dipartimento di Scienze e Tecnologie Aerospaziali, Politecnico di Milano, Italy

This paper deals with the active suppression of aerodynamically driven limit cycle flutters. Because of the significant dependence of such outcomes upon flight conditions, an adaptive solution is selected. The related task is accomplished through an Immersion and Invariance (I&I) controller coupled to a sliding mode observer. To simplify its tuning while satisfying robust stability conditions the design of the controller includes attenuating linear filters. The effect of using different fidelity approximations for the aerodynamic subsystem is verified on three different test cases, adopting reduced order models to design their controllers, including the dynamics of sensors and saturating actuators. The resulting active systems are subsequently verified against diverse nonlinear high fidelity aerodynamics, flight conditions and structural parameters.

Nomenclature

β_c	Control input
$\boldsymbol{\psi}$	Controller regressor
$\hat{\boldsymbol{\chi}}$	Uncertain parameter vector
λ, c_s, μ, γ_{Con}, σ, b_d	Controller design parameters
$\mathbf{A}_r$, $\mathbf{B}_r$, $\mathbf{C}_r$, $\mathbf{D}_r$	Reduced order matrices of the nonlinear aerodynamics
$\mathbf{f}_a$	Aerodynamic forces scaled by the dynamic pressure q_∞
$\mathbf{M}_a$, $\mathbf{C}_a$, $\mathbf{K}_a$	Aerodynamic quasi-steady approximation matrices
$\mathbf{M}_s$, $\mathbf{C}_s$, $\mathbf{K}_s$	Structural mass, damping and stiffness matrices
$\mathbf{q}$	Servo-elasto-mechanical degrees of freedom
$\mathbf{Q}$, $\mathbf{R}$, $\mathbf{Q}_s$, γ_{Obs}	Observer design parameters

*Ph.D. Candidate, Dipartimento di Scienze e Tecnologie Aerospaziali, Politecnico di Milano, Via La Masa 34, 20156 Milano, Italy.
†Professor, Dipartimento di Scienze e Tecnologie Aerospaziali, Politecnico di Milano, Via La Masa 34, 20156 Milano, Italy.

$\mathbf{q}_s$	Structural degrees of freedom
$\mathbf{x}_a$	Aerodynamic state
$\mathbf{z}$	Off-the-manifold variable
ω	Circular frequency
$\phi(v)$	Neural network activation function
ξ	Generalized damping ratio
b	Wing semi-chord
c	Wing chord
h, θ, β	Plunge, pitch and flap degrees of freedom
$J_{\beta\beta}$	Flap moment of inertia
$J_{\theta\theta}$	Airfoil/wing moment of inertia
$k = \dfrac{\omega b}{V_\infty}$	Reduced frequency
m	Airfoil/wing mass
N_a	Number of aerodynamic state
s	Control design target
$S_{h\beta}$	Flap static unbalance
$S_{h\theta}$	Airfoil/wing static unbalance
V_∞	Flight speed
$V_{\mathrm{F,OL}}$	Open loop flutter speed
x_h	Hinge position
y_a^{start}, y_a^{end}	Aileron span bounds

I. Introduction

The improvement of aircraft performances through active control is a well established research and industrial topic and it is likely that adaptive control systems will further enhance future airplanes stability and maneuverability [1,2]. Their development demands a comprehensive approach to appropriately deal with optimized designs, covering the whole spectrum of problems integrating flight mechanics and aeroservoelasticity, e.g.: flutter, control effectiveness and divergence, maneuver and gust loads, buffeting, flight performances [3]. Until the more recent decades, a somewhat inadequate computational power has restricted the ordinary study of aeroservoelastic systems to linear(ized) subsonic and supersonic flight regimes [4]. Nowadays, advances in computers technology and Computational Fluid Dynamics (CFD) allow to adequately evaluate nonlinear unsteady loads for inviscid and viscous flows. Therefore, the adoption of CFD-based aeroservoelastic analyses is becoming more and more viable [5], thus allowing to better deal with transonic flows and strong oscillating shocks. The full control of these, possibly dangerous, nonlinear events is of utmost importance in avoiding unacceptable self-induced oscillations, instabilities, limit cycles, ride-quality deterioration and fatigue failures [3]. Different approaches to the active control of aeroelastic systems can be found in the literature, to cite a few: classical LQG design [6], robust $\mathcal{H}_\infty$ framework [7], input limiting [8, 9], immersion and invariance [10], indirect adaption [11], adaptive neural networks, both static and recurrent [12–14]. Within such efforts, it is worth mentioning the comprehensive Benchmark Active Control Technology (BACT) research project, conducted at NASA Langley Research Center with the objective of measuring and archiving unsteady aerodynamics data in transonic flow. It has allowed to study, record, and experimentally validate a wide variety of active flutter suppression designs, such as: classical and minimax [15], robust $\mathcal{H}_\infty$ and $\mu-$synthesis [7], robust passification [16] and neural networks [12].

Given that aeroelastic systems change their stability with flight conditions, an efficient controller must work properly over the whole flight envelope of interest. To achieve such a result, two different approaches can be considered, i.e. scheduled and adaptive control. While the former requires many designs, covering a set of flight conditions adequate to insure a stable and smooth scheduling, the latter, once designed and verified for a relatively few peculiar cases, should be capable to adapt even to unforeseen conditions, with the likely added advantage of a reduced design effort.

In such a view this work adopts an Immersion and Invariance (I&I) approach [10, 17–22] for stabilising an aeroelastic system beyond its flutter speed. The related theory and a large number of applications to mechanical and aerospace systems, including airplanes trajectory tracking, can be found in [17, 18], while applications to spacecraft systems are referred in [19], where the concept of filter embedment is introduced for the first time. The adoption of an I&I methodology to relatively simple aeroelastic systems is considered in [10, 21, 22], where, assuming ideal actuators and the availability of the full state, both single and multiple input controllers are developed.

Here active flutter suppressors will be designed on realistic, linear and nonlinear, reduced order models, including sensors and actuators, the latter saturating in position, speed, and torque, verifying them afterward through high fidelity, CFD-based, simulations of the aerodynamic sub-system. Then, even if an I&I state observer formulation could be devised [17], a somewhat simpler and robust sliding mode scheme will be preferred for the implementation of the so designed controller.

The whole procedure will be verified through three test cases. At first the control of a simple pitching and plunging typical section, with a NACA 64A010 airfoil, is considered. This case is characterized by highly nonlinear unsteady aerodynamic loads, producing significant shock motions and a strong limit cycle oscillation, with a relatively high frequency. Moreover it allows to verify the importance of adequately modeling the dynamics of the adopted sensors and actuators. The second case considers the, already mentioned, Benchmark Active Control Technology (BACT) wing, with its fully validated models and data [7,15]. Because of its mild and low frequency flutter oscillations, it admits a linearized quasi-steady aerodynamic approximation for the design phase. Its model is also of the typical section kind but, being a true wing, the related high fidelity CFD verifications will provide a way to adequately check possible three dimensional effects. The third and final test considers the flexible Goland wing [23], with an added trailing edge control surface to make it possible its active flutter suppression. The related aerodynamics is quite simple, i.e an experimentally validated nonlinear quasi-steady strip theory [24]. Nevertheless, by providing a more complex three dimensional case with distributed elasticity, it allows to verify the proposed I&I controller on a more realistic system, characterized by a significant number of degrees of freedom.

The contribution of this paper lies in the development of a somewhat general approach to the adaptive stabilisation of nonlinear aeroelastic systems, considering high fidelity aerodynamics and saturating actuators. Moreover, the adoption of a time continuous nonlinear observer, along with the simulation of its digitalized implementation, addresses possible applications to even more realistic aeroelastic problems.

II. Aeroservoelastic models

An aeroservoelastic system is typically composed by three interconnected parts: structure, aerodynamics and control, and, depending on specific analysis and design needs, different model fidelities can be used in the various stages of its development. Following a standard approach, a generic linear(ized) structural model, can be discretizated into the classical multi-degrees of freedom scheme:

$$\mathbf{M}_s\ddot{\mathbf{q}}_s + \mathbf{C}_s\dot{\mathbf{q}}_s + \mathbf{K}_s\mathbf{q}_s = q_\infty\mathbf{f}_\mathrm{a} + \mathbf{T}_\beta^\mathrm{T}\mathbf{m}_\beta \tag{1}$$

where: $\mathbf{M}_s$, $\mathbf{C}_s$, $\mathbf{K}_s$ are the structural mass, damping and stiffness matrices, $\mathbf{q}_s$ the generalized structural coordinates, whose physical meaning is determined by the assumed discretization and $\mathbf{f}_\mathrm{a}$ the external generalized aerodynamic forces, scaled by the asymptotic dynamic pressure q_∞.

To explain the term $\mathbf{T}_\beta^\mathrm{T}\mathbf{m}_\beta$ in the above formula, it is remarked that the driving degree of freedom of any control surface is typically embedded in $\mathbf{q}_s$, so to be easily interfaced to the aerodynamic subsystem in the very same way as any other structural motion. Therefore, control surface rotations, $\boldsymbol{\beta}$, will be defined by $\boldsymbol{\beta} = \mathbf{T}_\beta\mathbf{q}_s$, $\mathbf{T}_\beta$ being an appropriate linking kinematic matrix, so that the generalized hinge moments, $\mathbf{m}_h$, associated to the external control moments, $\mathbf{m}_\beta$, will be given by $\mathbf{m}_h = \mathbf{T}_\beta^\mathrm{T}\mathbf{m}_\beta$.

After defining with $\mathcal{D}(\mathbf{v})$ the diagonal matrix associated to a vector $\mathbf{v}$, we assume that a set of position servos, commanding $\boldsymbol{\beta}$ to $\boldsymbol{\beta}_c$, can be adequately modeled as:

$$\begin{aligned}
&\ddot{\mathbf{x}}_{\mathrm{act}} + \mathcal{D}(2\xi_{\mathrm{act}}\omega_{\mathrm{act}})\dot{\mathbf{x}}_{\mathrm{act}} + \mathcal{D}(\omega_{\mathrm{act}}^2)\mathbf{x}_{\mathrm{act}} = \mathcal{D}(\omega_{\mathrm{act}}^2)\boldsymbol{\beta}_c \qquad \mathbf{m}_\beta = \mathcal{D}(\mathbf{k}_\beta)(\mathbf{x}_{\mathrm{act}} - \mathbf{T}_\beta\mathbf{q}_s) \\
&|\mathbf{x}_{\mathrm{act}}| \le \mathbf{x}_{\mathrm{act}_{\max}} \qquad |\dot{\mathbf{x}}_{\mathrm{act}}| \le \dot{\mathbf{x}}_{\mathrm{act}_{\max}} \qquad |\mathbf{m}_\beta| \le \mathbf{m}_{\beta_{\max}}
\end{aligned} \tag{2}$$

with ξ_{act} and ω_{act}^2 defining the actuator bandwidth, $\mathbf{k}_\beta$ an assumed acceptable low frequency residualization of their dynamic compliance, the 'max' suffixed terms indicating the related (symmetric) saturation values.

In view of the need of modeling only the transfer function of accelerometer based measures, the related acceleration output, at assigned locations, will be given by $\mathbf{a} = \mathbf{T}_a\ddot{\mathbf{q}}_s$, $\mathbf{T}_a$ being a suitable displacement interpolation matrix. Therefore, the related transducer dynamics (sensor, compensation, antialiasing filter) is approximated through:

$$\ddot{\mathbf{x}}_{\mathrm{sens}} + \mathcal{D}(2\xi_{\mathrm{sens}}\omega_{\mathrm{sens}})\dot{\mathbf{x}}_{\mathrm{sens}} + \mathcal{D}(\omega_{\mathrm{sens}}^2)\mathbf{x}_{\mathrm{sens}} = \mathcal{D}(\omega_{\mathrm{sens}}^2)\mathbf{a} = \mathcal{D}(\omega_{\mathrm{sens}}^2)\mathbf{T}_a\ddot{\mathbf{q}}_s \tag{3}$$

Finally, taking for granted its stability, a generic formulation of a linear-nonlinear unsteady aerodynamic subsystem is written as:

$$\dot{\mathbf{x}}_a = \mathbf{f}_{x_a}(\mathbf{x}_a, \mathbf{q}_s, \dot{\mathbf{q}}_s) \qquad \mathbf{f}_a = \mathbf{f}_a(\mathbf{x}_a, \mathbf{q}_s, \dot{\mathbf{q}}_s) \tag{4}$$

where $\mathbf{x}_a$ is the aerodynamic state, which can be either a physical entity, as in the case of a raw CFD model, or a generically abstract reduced order state.

Defining the extended servo-elasto-mechanical degrees of freedom $\mathbf{q} = [\mathbf{q}_s\ \mathbf{x}_{\mathrm{act}}\ \mathbf{x}_{\mathrm{sens}}]^{\mathrm{T}}$ and the corresponding state $\mathbf{x} = [\mathbf{q}\ \dot{\mathbf{q}}]^{\mathrm{T}} = [\mathbf{q}_s\ \mathbf{x}_{\mathrm{act}}\ \mathbf{x}_{\mathrm{sens}}\ \dot{\mathbf{q}}_s\ \dot{\mathbf{x}}_{\mathrm{act}}\ \dot{\mathbf{x}}_{\mathrm{sens}}]^{\mathrm{T}}$, putting together all of what above, we are led to the following nonlinear, strictly proper, state space formulation:

$$\begin{cases} \dot{\mathbf{x}} & = \mathbf{A}\mathbf{x} + \mathbf{B}_c\boldsymbol{\beta}_c + q_\infty\mathbf{B}_a\ \mathbf{f}_a(\mathbf{x}_a, \mathbf{q}_s, \dot{\mathbf{q}}_s) + \mathbf{B}_s\mathbf{u}_{\mathrm{sat}} \\ \mathbf{y} & = \mathbf{C}_y\mathbf{x} \end{cases} \qquad \dot{\mathbf{x}}_a = \mathbf{f}_{x_a}(\mathbf{x}_a, \mathbf{q}_s, \dot{\mathbf{q}}_s) \tag{5}$$

where $\mathbf{y}$ is a linear measure output and the other terms are defined through the following intermediate vectors and matrices[a]:

$$\mathbf{s}_\beta = \mathrm{linsat}(\mathbf{k}_\beta, \mathrm{linsat}(1, \mathbf{x}_{act}) - \boldsymbol{\beta}) \qquad \mathbf{s}_{\mathrm{act}} = \mathrm{linsat}(2\xi_{\mathrm{act}}\omega_{\mathrm{act}}, \dot{\mathbf{x}}_{\mathrm{act}}) + \mathrm{linsat}({\omega_{\mathrm{act}}}^2, \mathbf{x}_{\mathrm{act}}) \tag{6}$$

$$\mathbf{M} = \begin{bmatrix} \mathbf{M}_s & \mathbf{0} & \mathbf{0} \\ \mathbf{0} & \mathbf{I} & \mathbf{0} \\ -\mathcal{D}(\omega_{\mathrm{sens}}^2)\mathbf{T}_a & \mathbf{0} & \mathbf{I} \end{bmatrix} \quad \mathbf{C} = \begin{bmatrix} \mathbf{C}_s & \mathbf{0} & \mathbf{0} \\ \mathbf{0} & \mathcal{D}(2\xi_{\mathrm{act}}\omega_{\mathrm{act}}) & \mathbf{0} \\ \mathbf{0} & \mathbf{0} & \mathcal{D}(2\xi_{\mathrm{sens}}\omega_{\mathrm{sens}}) \end{bmatrix} \quad \mathbf{u}_{\mathrm{sat}} = \begin{Bmatrix} \mathbf{s}_\beta \\ \mathbf{s}_{\mathrm{act}} \end{Bmatrix} \tag{7}$$

[a] $\mathrm{linsat}(a, v) =: a\,v$ if $|v| \le v_{\max}$; $a\,v_{\max}$ if $v > v_{\max}$; $-a\,v_{\max}$ if $v < -v_{\max}$; the vector case must be intended component by component.

$$\mathbf{K} = \begin{bmatrix} (\mathbf{K}_s + \mathbf{T}_\beta^{\mathrm{T}} \mathcal{D}(\mathbf{k}_\beta) \mathbf{T}_\beta) & -\mathbf{T}_\beta^{\mathrm{T}} \mathcal{D}(\mathbf{k}_\beta) & \mathbf{0} \\ \mathbf{0} & \mathcal{D}(\omega_{\mathrm{act}}^2) & \mathbf{0} \\ \mathbf{0} & \mathbf{0} & \mathcal{D}(\omega_{\mathrm{sens}}^2) \end{bmatrix} \quad \mathbf{B}_{aq} = \begin{bmatrix} \mathbf{I} \\ \mathbf{0} \\ \mathbf{0} \end{bmatrix} \quad \mathbf{B}_{cq} = \begin{bmatrix} \mathbf{T}_\beta^{\mathrm{T}} \mathcal{D}(\mathbf{k}_\beta) \\ \mathbf{0} \\ \mathbf{0} \end{bmatrix} \quad \mathbf{B}_{sq} = \begin{bmatrix} \mathbf{I} & \mathbf{0} \\ \mathbf{0} & \mathbf{I} \\ \mathbf{0} & \mathbf{0} \end{bmatrix} \quad (8)$$

so that it is possible to set the following final compacted elements of Eq. 5:

$$\mathbf{A} = \begin{bmatrix} \mathbf{0} & \mathbf{I} \\ -\mathbf{M}^{-1}\mathbf{K} & -\mathbf{M}^{-1}\mathbf{C} \end{bmatrix} \quad \mathbf{B}_a = \begin{bmatrix} \mathbf{0} \\ \mathbf{M}^{-1}\mathbf{B}_{aq} \end{bmatrix} \quad \mathbf{B}_c = \begin{bmatrix} \mathbf{0} \\ \mathbf{M}^{-1}\mathbf{B}_{cq} \end{bmatrix} \quad \mathbf{B}_s = \begin{bmatrix} \mathbf{0} \\ \mathbf{M}^{-1}\mathbf{B}_{sq} \end{bmatrix} \quad (9)$$

$$\mathbf{C}_y = \begin{bmatrix} \mathbf{0} & \mathbf{0} & \mathbf{I} & \mathbf{0} & \mathbf{0} & \mathbf{0} \end{bmatrix} \quad (10)$$

It should be remarked that when high fidelity aerodynamic models are taken into account, $\mathbf{x}_a$ can be very large, so that the system size can be limited substantially only by using a reduced order aerodynamics. Therefore, whenever a high fidelity aerodynamic implies tens to hundreds of thousands states, the controller design will be based on a significantly more favourable ROM size.

III. Detailing the Adopted Aerodynamic Models

This work takes into account three different fidelity levels for the nonlinear aerodynamic sub-system: high fidelity CFD formulations, nonlinear reduced order models and linear-nonlinear quasi-steady approximations, which are briefly described below.

III.A. High fidelity CFD representation

The aerodynamic sub-system is modeled by a cell centered Finite-Volume (FV) scheme, using the aerodynamic code AeroFoam, developed at Dipartimento di Scienze e Tecnologie Aerospaziali, Politecnico di Milano [25]. AeroFoam is a density-based compressible Unsteady Euler/Reynolds-Averaged-Navier-Stokes (URANS-RANS) solver, the Euler option being selected in this work. Among its features there is an aeroelastic interfacing scheme, based on a Moving Least Squares (MLS) interpolation strategy, providing all the needed functionalities to set the appropriate aerodynamic boundary conditions imposed by a deforming structure, while driving a connected hierarchical mesh deformation within an Arbitrary Lagrangian Eulerian (ALE) formulation. An extended illustration of its aeroelastic capabilities can be found in [26]. In this work any of AeroFoam aerodynamic formulations can be synthesized in the form of Eq. 4, with $\mathbf{x}_a$ being the physical state associated to the FV cell centers, i.e. density, momentum, energy and the turbulence model own state. The generalized aerodynamic loads are computed through the integration of the pressure and viscous stresses on the body surface [25]. The high number of states (from tens of thousands to millions) required for an accurate approximation implies highly time demanding CFD-based analyses. Consequently, such simulations are mostly restricted to the verification phases of a design.

III.B. Reduced Order Models Through Recurrent Neural Networks

For classical linear(ized) flows, mostly based on the solution of an integral equation, linear identification methods can be exploited to provide a reduced order state space representation, see [27] and references therein. Even when the flow is nonlinear, e.g. Euler-based CFD codes, linear load identification methods can be adopted for small motions around a steady trimmed solution [28]. Nevertheless, when the structural system undergoes large enough motions, causing significant changes of the flow field, e.g. moving shocks, an unsteady, nonlinear aerodynamic model of the type previously described is required. As already remarked, it can provide a high level of fidelity only at the cost of a significantly fine discretization, with the related demand of computational power and time consuming simulations. This fact limits its applicability to control designs, sensitivity studies and system optimization, for which a Reduced Order Model (ROM) is almost compulsory [29]. Different approaches for the determination of nonlinear aerodynamic ROMs are available in the literature, e.g. Proper Orthogonal Decomposition [28, 30], Volterra series [31, 32] and Kriging-based surrogate models [33].

In this work it has been chosen to exploit a Continuous Time Recurrent Neural Network (CTRNN) [34]. After defining the structural only state with $\mathbf{x}_s = [\mathbf{q}_s \ \dot{\mathbf{q}}_s]^{\mathrm{T}}$, the related stable aerodynamic ROM can be appropriately defined with the following ordinary differential equations:

$$\dot{\mathbf{x}}_a = \mathbf{A}_r \boldsymbol{\phi}(\mathbf{x}_a) + \mathbf{B}_r \mathbf{x}_s \qquad\qquad \mathbf{f}_a = \mathbf{C}_r \boldsymbol{\phi}(\mathbf{x}_a) + \mathbf{D}_r \mathbf{x}_s \tag{11}$$

where $\phi : \mathbb{R}^{N_a} \rightarrow \mathbb{R}^{N_a}$ is a function vector whose elements are hyperbolic tangent functions, i.e. $\phi_i(x) = \tanh x$. The matrices $\mathbf{A}_r$, $\mathbf{B}_r$, $\mathbf{C}_r$, $\mathbf{D}_r$ contain the network synaptic weights, which are tuned through a sequential training procedure based on an optimization scheme organized in two levels. The first, which initializes the coefficients, is based on a Genetic Algorithm minimizing a quadratic cost function of the identification error: $F = \dfrac{1}{2}\sum_{i=1}^{N_t} ||\mathbf{f}_{a,\mathrm{ROM}}(t_i) - \mathbf{f}_{a,\mathrm{CFD}}(t_i)||^2$, where N_t is the number of training samples considered. A good compromise between an acceptable accuracy at the end of this phase and its computational time can be achieved by setting the probability of mutation approximately at 0.15, along with a maximum of 150 generations. The range of values within which the synaptic weights are allowed to vary is $[-10, 10]$. Instead, starting from the best population resulting from the initialization phase, the second training level exploit the Levenberg-Marquardt algorithm, for the same cost function, eventually driving the identification error to a desired converged precision at a faster pace.

The training signals are generated within the previously described CFD solver. Sequences of ramps are considered for all the structural degrees of freedom, choosing the time length of each ramp in relation to a set of reduced frequencies that must be excited to obtain a sufficiently accurate ROM. The time length any ramp, Δr, is related to the reduced frequency of interest through the relation $\Delta r = \frac{2\,\pi\,c}{V_\infty\,k}$. In practice, different training sequences are considered, starting from filtered smooth ramp signals and ending with barely blended ramps. Because of the presence of both steady-state and transient responses, this approach has proved capable of improving the learning capability of the CTRNN for an aeroelastically coupled fine CFD grid, as exemplified in Figure 1.

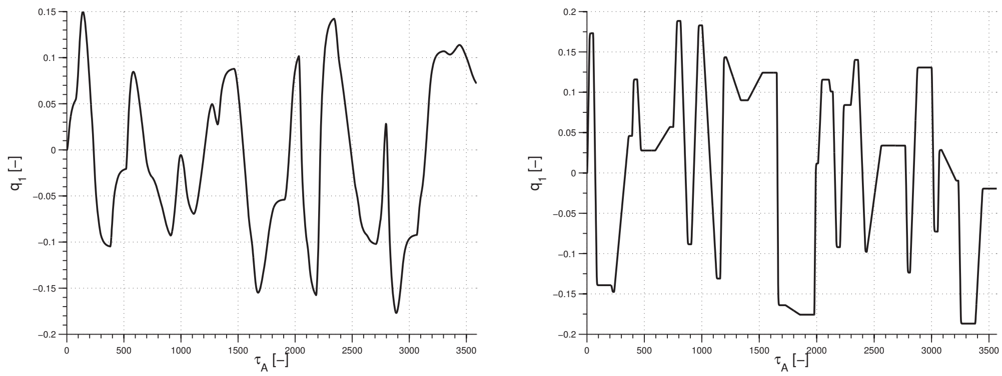

(a) Smoothed ramp sequence. (b) Slightly blended ramp sequence.

Figure 1: Sample of the signals used in the training phase of a neural network based ROM.

III.C. Quasi-Steady Approximation

In the case of low frequency structural motions, i.e. for reduced frequencies somewhat smaller than 0.1, the aerodynamic response to structurally imposed boundary conditions can be retained sufficiently fast to make it acceptable a quasy steady residualization of $\mathbf{f}_a$ within a limited range of low reduced frequencies [35, 36]. Within such an assumption, the generalized aerodynamic forces can be approximated in the following way:

$$\mathbf{f}_a\left(\mathbf{q}_s, \dot{\mathbf{q}}_s, \ddot{\mathbf{q}}_s\right) = \left(\frac{c}{2\,V_\infty}\right)^2 \mathbf{M}_a \ddot{\mathbf{q}}_s + \frac{c}{2\,V_\infty} \mathbf{C}_a \dot{\mathbf{q}}_s + \mathbf{K}_a \mathbf{q}_s + \mathbf{f}_{a_{\mathrm{nl}}}(\mathbf{q}_s, \dot{\mathbf{q}}_s) \tag{12}$$

the nonlinear term, $\mathbf{f}_{\mathrm{a_{nl}}}$, introducing any appropriate non linear quasi-steady correction. Sometimes, the values used in the above rough approximation can be improved and tuned to match available experimental data, as in the case of the following BACT and Goland wing [37, 38] applications.

IV. Control Methodology

IV.A. Immersion and Invariance adaptive controller

Controllers based on the Immersion and Invariance (I&I) into stable manifolds are a somewhat novel concept. The related theory can be found in [17], while some applications to aeroelastic systems are reported in [10, 21, 22]. The filter embedment approach adopted here can be found in [19, 20]. The basic I&I idea is to achieve a stabilisation by immersing the plant dynamics into a stable target system, possibly described by a reduced number of states. Then, by introducing appropriate adaptive terms in the related controller, it is possible to achieve the invariance of the manifold containing such a target [18].

In this work the target system will be represented by:

$$s = \dot{\tilde{y}} + \lambda\tilde{y} \tag{13}$$

λ being a positive tunable design parameter and $\tilde{y}$ the controlled target performance, which can be any linear combination of the system state components. Anticipating that only the displacement at a key point of the structure will be taken into account in this work, we can write:

$$\tilde{y} = \mathbf{H}\mathbf{x} = \begin{bmatrix} \mathbf{H}_q & \mathbf{0} \end{bmatrix} \begin{Bmatrix} \mathbf{q} \\ \dot{\mathbf{q}} \end{Bmatrix} = \mathbf{H}_q\mathbf{q} \tag{14}$$

with $\mathbf{H}$ and $\mathbf{H}_q$ defining the appropriate single line target output matrix, specified on a case by case basis to define the desired $\tilde{y}$. It must be remarked that, since we aim at a stabilization through a single control input, a multi components target will result in a singular controller. It would nevertheless be possible to take into account any additional performance of interest, but, as shown in [22], the number of control input must be increased accordingly. Since the performance dynamics must be asymptotically stable over the manifold $s = 0$, it is sufficient to develop a control law driving s to the origin. By differentiating Eq. 13, the dynamics of s is driven by the following equation:

$$\dot{s} = \ddot{\tilde{y}} + \lambda\dot{\tilde{y}} \tag{15}$$

where the required $\tilde{y}$ derivatives are explicitly defined through:

$$\begin{aligned} \dot{\tilde{y}} &= \mathbf{HAx} + q_\infty\mathbf{HB}_a\mathbf{f}_a + \mathbf{HB}_s\mathbf{u}_{\text{sat}} + \mathbf{HB}_c\beta_c = \mathbf{HAx} = \mathbf{H}_q\dot{\mathbf{q}} \\ \ddot{\tilde{y}} &= \mathbf{HA}^2\mathbf{x} + q_\infty\mathbf{HAB}_a\mathbf{f}_a + \mathbf{HAB}_s\mathbf{u}_{\text{sat}} + \mathbf{HAB}_c\beta_c \end{aligned} \tag{16}$$

The omission of the terms containing $\mathbf{B}_a$, $\mathbf{B}_s$ and $\mathbf{B}_c$ in the first equation above can be trivially inferred by looking at their definitions against that of $\mathbf{H}$. Therefore Eq. 15 becomes:

$$\begin{aligned}\dot{s} &= \mathbf{H}\mathbf{A}^2\mathbf{x} + q_\infty \mathbf{H}\mathbf{A}\mathbf{B}_a\mathbf{f}_a + \mathbf{H}\mathbf{A}\mathbf{B}_s\mathbf{u}_{\mathrm{sat}} + \mathbf{H}\mathbf{A}\mathbf{B}_c\beta_c + \lambda\mathbf{H}_q\dot{\mathbf{q}} \\ &= \mathbf{x}^{\mathrm{T}}\boldsymbol{\alpha} + q_\infty\mathbf{f}_a^{\mathrm{T}}\boldsymbol{\omega} + \mathbf{u}_{\mathrm{sat}}^{\mathrm{T}}\boldsymbol{\gamma} + b\beta_c + \lambda\mathbf{H}_q\dot{\mathbf{q}}\end{aligned} \tag{17}$$

with: $\boldsymbol{\alpha} = \left(\mathbf{H}\mathbf{A}^2\right)^{\mathrm{T}}$, $\boldsymbol{\omega} = \left(\mathbf{H}\mathbf{A}\mathbf{B}_a\right)^{\mathrm{T}}$, $\boldsymbol{\gamma} = \left(\mathbf{H}\mathbf{A}\mathbf{B}_s\right)^{\mathrm{T}}$ and $b = \mathbf{H}\mathbf{A}\mathbf{B}_c$, being unknown constant parameters, except for the sign of b, which is assumed as known. Then, after defining the positive design parameter c_s, an asymptotically stable manifold is enforced by adding and subtracting the term $c_s s$ to Eq. 15, obtaining:

$$\begin{aligned}\dot{s} &= \mathbf{x}^{\mathrm{T}}\boldsymbol{\alpha} + q_\infty\mathbf{f}_a^{\mathrm{T}}\boldsymbol{\omega} + \mathbf{u}_{\mathrm{sat}}^{\mathrm{T}}\boldsymbol{\gamma} + b\beta_c + \lambda\mathbf{H}_q\dot{\mathbf{q}} + c_s s - c_s s \\ &= -c_s s + b\left[\beta_c + \mathbf{x}^{\mathrm{T}}b^{-1}\boldsymbol{\alpha} + q_\infty\mathbf{f}_a^{\mathrm{T}}b^{-1}\boldsymbol{\omega} + \mathbf{u}_{\mathrm{sat}}^{\mathrm{T}}b^{-1}\boldsymbol{\gamma} + b^{-1}\left(\lambda\mathbf{H}_q\dot{\mathbf{q}} + c_s s\right)\right]\end{aligned} \tag{18}$$

After defining the following vectors:

$$\hat{\boldsymbol{\chi}} = \begin{bmatrix} b^{-1}\boldsymbol{\alpha} & b^{-1}\boldsymbol{\omega} & b^{-1}\boldsymbol{\gamma} & b^{-1}\end{bmatrix}^{\mathrm{T}} \qquad \boldsymbol{\psi} = \begin{bmatrix}\mathbf{x} & q_\infty\mathbf{f}_a\left(\mathbf{x}_a, \mathbf{q}_s, \dot{\mathbf{q}}_s\right) & \mathbf{u}_{\mathrm{sat}} & \left(\lambda\mathbf{H}_q\dot{\mathbf{q}} + c_s s\right)\end{bmatrix}^{\mathrm{T}} \tag{19}$$

Eq. 18 can be written in the following compacted form:

$$\dot{s} = -c_s s + b\left(\beta_c + \boldsymbol{\psi}^{\mathrm{T}}\hat{\boldsymbol{\chi}}\right) \tag{20}$$

In order to somewhat simplify the I&I design procedure presented in Ref. [17], $s = \mathbf{H}_q\left(\dot{\mathbf{q}} + \lambda\,\mathbf{q}\right)$, $\boldsymbol{\psi}$ and β_c are low pass filtered and attenuated [19–21] in accordance with the following equations:

$$\text{a)}\quad \dot{s}_f = -\mu s_f + \mathbf{H}_q\left(\dot{\mathbf{q}} + \lambda\,\mathbf{q}\right) \qquad \text{b)}\quad \dot{\boldsymbol{\psi}}_f = -\mu\boldsymbol{\psi}_f + \boldsymbol{\psi} \qquad \text{c)}\quad \dot{\beta}_{c,f} = -\mu\beta_{c,f} + \beta_c \tag{21}$$

where μ is a further positive design parameter. Given that the proposed linear filters are asymptotically stable, it can be shown [21] that the following ordinary differential equation is satisfied asymptotically:

$$\dot{s}_f = -c_s s_f + b\left(\beta_{c,f} + \boldsymbol{\psi}_f^{\mathrm{T}}\hat{\boldsymbol{\chi}}\right) \tag{22}$$

Since $\hat{\boldsymbol{\chi}}$ is unknown, I&I approximates it through the aid of shaping terms which will force the stable manifold to be invariant. Within such a view, we define the off-the-manifold variable $\mathbf{z}$ [17]:

$$\mathbf{z} = \left(\boldsymbol{\chi} + \boldsymbol{\delta}\right) - \hat{\boldsymbol{\chi}} \tag{23}$$

with $\boldsymbol{\delta}(s_f, \boldsymbol{\psi}_f)$ being a yet to be chosen shaping function, so that, defining a control law of the form $\beta_{c,f} = -\boldsymbol{\psi}_f^{\mathrm{T}}\left(\mathbf{z} + \hat{\boldsymbol{\chi}}\right)$, it is possible to cancel the unknown constant parameter vector $\hat{\boldsymbol{\chi}}$ of Eq. 22, which becomes:

$$\dot{s}_f = -c_s s_f - b\boldsymbol{\psi}_f^{\mathrm{T}}\mathbf{z} \tag{24}$$

As a side note we remark that for $\boldsymbol{\delta} = \mathbf{0}$ Eq. 23 recovers the classical formulation of a certainty-equivalent adaptive controller [39]. Because of Eq. 23 we have also $\beta_{c,f} = -\boldsymbol{\psi}_f^{\mathrm{T}}(\boldsymbol{\chi} + \boldsymbol{\delta})$, so that, recalling Eq. 21 b) and $\dot{\hat{\boldsymbol{\chi}}} = \mathbf{0}$, $\dot{\beta}_{c,f} = \mu\boldsymbol{\psi}_f^{\mathrm{T}}(\boldsymbol{\chi} + \boldsymbol{\delta}) - \boldsymbol{\psi}^{\mathrm{T}}(\boldsymbol{\chi} + \boldsymbol{\delta}) - \boldsymbol{\psi}_f^{\mathrm{T}}\dot{\mathbf{z}}$. Therefore, using Eq. 21 c) we can write our control law $\beta_c = \mu\beta_{c,f} + \dot{\beta}_{c,f}$ as:

$$\text{a)} \quad \beta_c = -\boldsymbol{\psi}^{\mathrm{T}}(\boldsymbol{\chi} + \boldsymbol{\delta}) - \boldsymbol{\psi}_f^{\mathrm{T}}\dot{\mathbf{z}} \qquad \text{or} \qquad \text{b)} \quad \beta_c = -\boldsymbol{\psi}^{\mathrm{T}}(\boldsymbol{\chi} + \boldsymbol{\delta}) - \boldsymbol{\psi}_f^{\mathrm{T}}\left(\dot{\boldsymbol{\chi}} + \dot{\boldsymbol{\delta}}\right) \tag{25}$$

thus making $\beta_{c,f}$ useless.

In view of ensuring the asymptotic stability of $\mathbf{z}$ we take its time derivative:

$$\dot{\mathbf{z}} = \dot{\boldsymbol{\chi}} + \frac{\partial\boldsymbol{\delta}}{\partial s_f}\dot{s}_f + \frac{\partial\boldsymbol{\delta}}{\partial\boldsymbol{\psi}_f}\dot{\boldsymbol{\psi}}_f = \dot{\boldsymbol{\chi}} + \frac{\partial\boldsymbol{\delta}}{\partial s_f}\left(-c_s s_f - b\boldsymbol{\psi}_f^{\mathrm{T}}\mathbf{z}\right) + \frac{\partial\boldsymbol{\delta}}{\partial\boldsymbol{\psi}_f}\dot{\boldsymbol{\psi}}_f \tag{26}$$

so that, imposing the following adaptive definition of $\boldsymbol{\chi}$:

$$\dot{\boldsymbol{\chi}} = c_s s_f \frac{\partial\boldsymbol{\delta}}{\partial s_f} - \frac{\partial\boldsymbol{\delta}}{\partial\boldsymbol{\psi}_f}\dot{\boldsymbol{\psi}}_f \tag{27}$$

the dynamics of $\mathbf{z}$ is given by:

$$\dot{\mathbf{z}} = -\frac{\partial\boldsymbol{\delta}}{\partial s_f} b\boldsymbol{\psi}_f^{\mathrm{T}}\mathbf{z} \tag{28}$$

Defining $V_z = \frac{1}{2}\mathbf{z}^{\mathrm{T}}\mathbf{z}$ we have:

$$\dot{V}_z = \mathbf{z}^{\mathrm{T}}\dot{\mathbf{z}} = -\mathbf{z}^{\mathrm{T}}\frac{\partial\boldsymbol{\delta}}{\partial s_f} b\boldsymbol{\psi}_f^{\mathrm{T}}\mathbf{z} \tag{29}$$

which, after setting $\frac{\partial\boldsymbol{\delta}}{\partial s_f} = \gamma_{\mathrm{Con}}\mathrm{sign}\,(b)\,\boldsymbol{\psi}_f$, γ_{Con} being a positive design parameter, becomes:

$$\dot{V}_z = \mathbf{z}^{\mathrm{T}}\dot{\mathbf{z}} = -\gamma_{\mathrm{Con}}\,|b|\,\mathbf{z}^{\mathrm{T}}\boldsymbol{\psi}_f\boldsymbol{\psi}_f^{\mathrm{T}}\mathbf{z} = -\gamma_{\mathrm{Con}}\,|b|\,||\boldsymbol{\psi}_f^{\mathrm{T}}\mathbf{z}||^2 \tag{30}$$

thus ending with:

$$\dot{\mathbf{z}} = -\gamma_{\mathrm{Con}}\,|b|\,\boldsymbol{\psi}_f\boldsymbol{\psi}_f^{\mathrm{T}}\mathbf{z} \tag{31}$$

Therefore, $\mathbf{z} = \mathbf{0}$ is an uniformly stable equilibrium point, with $\mathbf{z} \in \mathcal{L}_\infty(0,\infty)$. Moreover, integrating $\dot{V}_z$ we obtain:

$$V_z(\infty) - V_z(0) = -\gamma_{\mathrm{Con}}\,|b|\int_0^\infty ||\boldsymbol{\psi}_f^{\mathrm{T}}\mathbf{z}||^2\,dt \tag{32}$$

and consequently $||\boldsymbol{\psi}_f^{\mathrm{T}}\mathbf{z}|| \in \mathcal{L}_2(0,\infty)$. Finally, integrating $\frac{\partial\boldsymbol{\delta}}{\partial s_f}$ with respect to s_f we can determine the expression of the shaping function:

$$\boldsymbol{\delta} = \gamma_{\mathrm{Con}}\,\mathrm{sign}\,(b)\;s_f\boldsymbol{\psi}_f \tag{33}$$

along with the time derivatives needed to complete Eq. 27 and Eq. 25 b), i.e.:

$$\dot{\boldsymbol{\chi}} = \left[-\boldsymbol{\psi} + \boldsymbol{\psi}_f\,(c_s+\mu)\right]\gamma_{\text{Con}}\,\text{sign}\,(b)\;s_f \tag{34}$$

$$\dot{\boldsymbol{\chi}} + \dot{\boldsymbol{\delta}} = \gamma_{\text{Con}}\,\text{sign}\,(b)\,\boldsymbol{\psi}_f^{\text{T}}\boldsymbol{\psi}_f\left[\mathbf{H}_q\left(\dot{\mathbf{q}} + \lambda\,\mathbf{q}\right) + (c_s-\mu)s_f\right] \tag{35}$$

We can then proceed and verify the stability of s_f by defining the following Lyapunov function $V_s = \dfrac{1}{2}s_f^2$, whereas, evaluating its time derivative and using Young's inequality, we have:

$$\begin{aligned}\dot{V}_s = s_f\,\dot{s}_f = -c_s s_f^2 - b\,s_f\,\boldsymbol{\psi}_f^{\text{T}}\mathbf{z} \leq -c_s s_f^2 + |b|\,|s_f|\,||\boldsymbol{\psi}_f^{\text{T}}\mathbf{z}||\\ \leq -c_s s_f^2 + \frac{c_s}{2}|s_f|^2 + \frac{|b|}{2c_s}||\boldsymbol{\psi}_f^{\text{T}}\mathbf{z}||^2 \leq -\frac{1}{2}c_s s_f^2 + \frac{|b|}{2c_s}||\boldsymbol{\psi}_f^{\text{T}}\mathbf{z}||^2\end{aligned} \tag{36}$$

Therefore, since $||\boldsymbol{\psi}_f^{\text{T}}\mathbf{z}|| \in \mathcal{L}_2\,(0,\infty)$, we have also $s_f \in \mathcal{L}_2\,(0,\infty)$, thus proving the asymptotic stability of s_f. To demonstrate the asymptotic stability of the whole control system, we resort to a third Lyapunov function: $W(s_f,\mathbf{z}) = V_s + V_z$, so that, being:

$$\dot{W} \leq -\frac{c_s}{2}s_f^2 - \left(\gamma_{\text{Con}} - \frac{1}{2c_s}\right)|b|\;||\psi_f^{\text{T}}\mathbf{z}||^2 \tag{37}$$

it can be inferred that the pair $(s_f,\mathbf{z}) \in \mathcal{L}_\infty(0,\infty)$, if $\gamma_{\text{Con}} \geq 1/(2c_s)$. In practice, the following inequality will be imposed:

$$2c_s\gamma_{\text{Con}} \geq \text{b}_d \tag{38}$$

with b_d being an assigned design bound. Given that the linear filters in Eq. 21 are all asymptotically stable, if s_f is bounded also s is and, consequently, $\tilde{y}$. Then, the whole state will be bounded and, since W is uniformly continuous, the convergence toward the origin can be proved by using Barbalat's lemma [39].

Putting together Eqs. 21, a) and b), Eq. 34, modified as shortly explained, finishing Eq. 25 by using Eq. 35, it is now possible to resume the nonlinear adaptive compensator and its control command:

$$\dot{s}_f = -\mu s_f + \mathbf{H}_q\left(\dot{\mathbf{q}}_o + \lambda\,\mathbf{q}_o\right) \qquad \dot{\boldsymbol{\psi}}_f = -\mu\boldsymbol{\psi}_f + \boldsymbol{\psi}_o \qquad \dot{\boldsymbol{\chi}} = -\sigma\boldsymbol{\chi} + \gamma_{\text{Con}}\,\text{sign}\,(b)\;s_f\left[-\boldsymbol{\psi}_o + \boldsymbol{\psi}_f\,(c_s+\mu)\right] \tag{39}$$

$$\beta_c = -\boldsymbol{\psi}^{\text{T}}\left(\boldsymbol{\chi} + \boldsymbol{\delta}\right) - \gamma_{\text{Con}}\,\text{sign}\,(b)\,\boldsymbol{\psi}_f^{\text{T}}\boldsymbol{\psi}_f\left[\mathbf{H}_q\left(\dot{\mathbf{q}}_o + \lambda\,\mathbf{q}_o\right) + (c_s-\mu)s_f\right] \tag{40}$$

where the suffix o indicates that the related quantities are computed using the values that will be provided by the sliding observer described in the following paragraph. As anticipated above we remark that the last of the Eqs. 39 has been modified, with respect to its parent Eq. 34, by adding an appropriate proportional feedback $-\sigma\boldsymbol{\chi}$, $\sigma > 0$ being a new design parameter. Such a change is an often used fix [40] aimed at avoiding a possible long term drift associated to pure integrations of the kind of Eq. 34, eventually hindering the previously demonstrated convergence and stability properties [41] because of unmodeled dynamics and disturbances. The stability improvement brought in by $-\sigma\boldsymbol{\chi}$ can be found in [40–42]. It is then possible to tune σ so to provide an acceptable trade-off between the nominal adaption performances and a sizeable robustness gain against the mentioned uncertainties and disturbances. It is further remarked, as reported in [21], that the so designed controller has the interesting feature that, defining the manifold Ω as:

$$\Omega = \left\{ \left(\boldsymbol{\psi}_f, \mathbf{z}\right) \,:\, \boldsymbol{\psi}_f^{\mathrm{T}} \mathbf{z} = 0 \right\} \tag{41}$$

the closed loop system is confined within Ω, with $\dot{s}_f = -c_s s_f$ on Ω. Such a result could also have been obtained through the deterministic control law $\beta_{c,f} = -\boldsymbol{\psi}_f^{\mathrm{T}} \boldsymbol{\chi}$, with $\boldsymbol{\chi}$ known. Therefore, thanks the inclusion of the additional shaping term $\boldsymbol{\delta}$, it follows that an I&I based controller asymptotically recovers the performances of a deterministic controller.

Under the constraint of Eq. 38, the meaning of the four design parameters λ, c_s, μ and γ_{Con} should be quite clear: λ drives the performance to zero when the target manifold is reached, c_s modulates the convergence toward the stable manifold, μ determines the filtering level of the controller and γ_{Con} modulates the control effort.

IV.B. Sliding Mode Observer

The previously described I&I controller requires the availability of the system state for its implementation. Thanks to the assumed smooth monotonic nonlinearities of the models here employed, a separation principle can be exploited [43], so any observer based implementation can be carried out without regard to the controller design. Moreover, since the significant differences between the design and verification models may cause system instabilities and performance degradation, it has then been decided to resort to a robust sliding mode observer. At first the method of reference [44] was successfully adopted. Nevertheless, while practicing with its design, it appeared that the resulting observer did not change significantly the aerodynamic eigenvalues, thus suggesting that the related reduced order aerodynamic state was more detectable than observable. So, after verifying that it provided equivalent results, a simpler scheme was chosen. It allows the direct use of a CTRNN based stable aerodynamic ROM without the need of any linearization and, recalling Eq. 5, has the form:

$$\begin{cases} \dot{\mathbf{x}}_o = \mathbf{A}\mathbf{x}_o + \mathbf{L}_{\mathrm{Obs}}\mathbf{e}_o + \mathbf{B}_c\,\beta_c + \mathbf{B}_s\mathbf{u}_{\mathrm{sat}_o} + q_\infty \mathbf{B}_a\,\mathbf{f}_a\left(\mathbf{x}_{a_o}, \mathbf{q}_{s_o}, \dot{\mathbf{q}}_{s_o}\right) + \mathbf{v}_s \\ \dot{\mathbf{x}}_{a_o} = \mathbf{f}_{x_a}\left(\mathbf{x}_{a_o}, \mathbf{q}_{s_o}, \dot{\mathbf{q}}_{s_o}\right) \end{cases} \tag{42}$$

where $\mathbf{v}_s$ is the to be designed sliding contribution, $\mathbf{e}_o = \mathbf{y} - \mathbf{C}_y\mathbf{x}_o$ the output error, $\mathbf{x}_o$ and $\mathbf{x}_{a_o}$ are, respectively, the observed servo-elasto-mechanical and aerodynamic state, with the observed structural generalized coordinates, $\mathbf{q}_{s_o}$ and $\dot{\mathbf{q}}_{s_o}$, being just the related partitions of $\mathbf{x}_o$. The observation gain $\mathbf{L}_{\mathrm{Obs}}$ is computed through a standard linear optimal asymptotic Kalman observer, designed through the solution of the algebraic Riccati equation:

$$\begin{cases} \mathbf{A}\mathbf{\Lambda} + \mathbf{\Lambda}\mathbf{A}^{\mathrm{T}} - \mathbf{\Lambda}\mathbf{C}_y^{\mathrm{T}}\mathbf{R}^{-1}\mathbf{C}_y\mathbf{\Lambda} + \mathbf{Q} = \mathbf{0} \\ \mathbf{L}_{\mathrm{Obs}} = -\mathbf{\Lambda}\mathbf{C}_y^{\mathrm{T}}\mathbf{R}^{-1} \end{cases} \tag{43}$$

with $\mathbf{Q}$ being a positive semi-definite design covariance of the system disturbances and $\mathbf{R}$ a positive definite design covariance related to measurement noise.

To determine $\mathbf{v}_s$ we resort to the dynamics of the state observation error, $\mathbf{e}(t) = \mathbf{x} - \mathbf{x}_o$:

$$\dot{\mathbf{e}} = (\mathbf{A} - \mathbf{L}_{\mathrm{Obs}}\mathbf{C}_y)\,\mathbf{e} - \mathbf{v}_s + \mathbf{B}_{\boldsymbol{\zeta}}\boldsymbol{\zeta} \tag{44}$$

with $\boldsymbol{\zeta}$ being a overall disturbance vector, summing up all the disturbances and uncertainties of the system.

The discontinuous switching vector $\mathbf{v}_s(t)$ of Eq. 42 is then determined by satisfying the stability condition associated to the Lyapunov function $V_{\mathrm{Obs}} = \mathbf{e}^{\mathrm{T}}\mathbf{T}\mathbf{e}$, for which we have:

$$\dot{V}_{\mathrm{Obs}} = \dot{\mathbf{e}}^{\mathrm{T}}\mathbf{T}\mathbf{e} + \mathbf{e}^{\mathrm{T}}\mathbf{T}\dot{\mathbf{e}} = -\mathbf{e}^{\mathrm{T}}\left((\mathbf{A} - \mathbf{L}_{\mathrm{Obs}}\mathbf{C}_y)^{\mathrm{T}}\,\mathbf{T} + \mathbf{T}\,(\mathbf{A} - \mathbf{L}_{\mathrm{Obs}}\mathbf{C}_y)\right)\mathbf{e} - 2\mathbf{v}_s^{\mathrm{T}}\mathbf{T}\mathbf{e} + 2\boldsymbol{\zeta}^{\mathrm{T}}\mathbf{B}_{\boldsymbol{\zeta}}^{\mathrm{T}}\mathbf{T}\mathbf{e} \tag{45}$$

Therefore, after assigning an appropriate positive-definite matrix $\mathbf{Q}_s$ and solving the following Lyapunov equation:

$$(\mathbf{A} - \mathbf{L}_{\mathrm{Obs}}\mathbf{C}_y)^{\mathrm{T}}\,\mathbf{T} + \mathbf{T}\,(\mathbf{A} - \mathbf{L}_{\mathrm{Obs}}\mathbf{C}_y) + \mathbf{Q}_s = \mathbf{0} \tag{46}$$

the sliding vector is designed to be

$$\mathbf{v}_s(t) = \begin{cases} -\gamma_{\mathrm{Obs}}\dfrac{\mathbf{T}\mathbf{e}}{||\mathbf{T}\mathbf{e}||} & \text{if } ||\mathbf{e}|| \neq 0 \\ 0 & \text{if } ||\mathbf{e}|| = 0 \end{cases} \tag{47}$$

so that, proceeding with Eq. 45 we have:

$$\dot{V}_{\mathrm{Obs}} \leq -\mathbf{e}^{\mathrm{T}}\mathbf{Q}_s\mathbf{e} - 2\gamma_{\mathrm{Obs}}||\mathbf{T}\mathbf{e}|| + 2||\mathbf{T}\mathbf{e}||||\mathbf{B}_{\boldsymbol{\zeta}}\boldsymbol{\zeta}|| \leq -\mathbf{e}^{\mathrm{T}}\mathbf{Q}_s\mathbf{e} - 2\lambda_{\max}(\mathbf{T})\left(\gamma_{\mathrm{Obs}} - \bar{\zeta}\right)||\mathbf{e}|| < 0 \tag{48}$$

where $\lambda_{\max}(\mathbf{T})$ is the maximum eigenvalue of $\mathbf{T}$ and $\bar{\zeta} = \sup(||\mathbf{B}_{\boldsymbol{\zeta}}\boldsymbol{\zeta}||)$ the estimated worst disturbance level. Since $\mathbf{e}$ is not available, it is computed by pseudo inverting the relation $\mathbf{e}_o = \mathbf{C}_y\mathbf{e}$, obtaining $\mathbf{e} = \mathbf{C}_y^{\mathrm{T}}\left(\mathbf{C}_y\mathbf{C}_y^{\mathrm{T}}\right)^{-1}\mathbf{e}_o$, which, because of the structure of our $\mathbf{C}_y$, becomes the simpler $\mathbf{e} = [\mathbf{0}\ \mathbf{0}\ \mathbf{x}_{\mathrm{sens}}\ \mathbf{0}\ \mathbf{0}\ \mathbf{0}]^{\mathrm{T}}$. As it is well known [44], the switching term aims at inducing a sliding motion in the state error space $\mathcal{S}_o = \{\mathbf{e} \in \mathbb{R}^n : \mathbf{C}_y\mathbf{e} = \mathbf{0}\}$, driving it to zero in a finite time. Despite the presence of modeling uncertainties, first and foremost, but not only, the approximations implied in $\mathbf{f}_a$, such a behavior can be achieved through an appropriate tuning of $\mathbf{Q}_s$, γ_{Obs} and $\bar{\zeta}$.

Figure 2 presents a few results obtained when the proposed observer is applied to an aerodynamically nonlinear typical section case, to be shown later. It evidences that an appropriate, rather easy, tuning of the observer design parameters results in a fast and accurate estimation of the systems state. In fact, because of the filtering action of the integration, the state error will be significantly smaller than that of the reconstructed acceleration. A digital implementation of the just presented observer is found in the following paragraph.

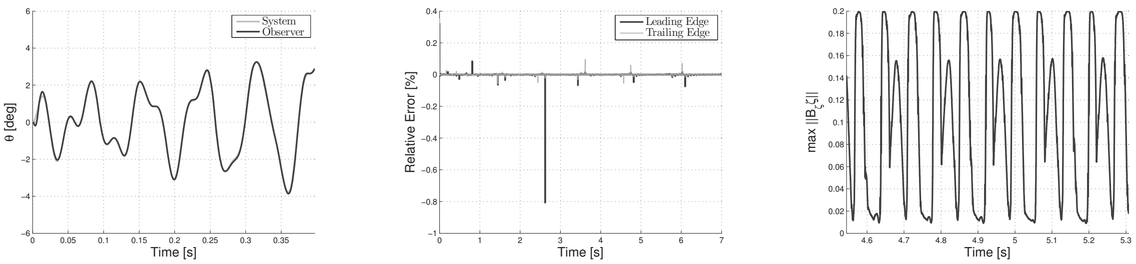

(a) $\gamma_{\text{Obs}} = 0.1$, pitch estimation. (b) Estimated accelerometric error. (c) State error dynamics ($\bar{\zeta}$).

Figure 2: Sample results of the sliding mode observer.

V. A Few Design Simulations

Apart from a specific change to the actuator bandwidth of the first test case, the parameters shared by all the accelerometers and actuators of the following applications are summarized in Table 1. The

	ξ	ω_0 [rad/s]	$\beta_{\max}$ [deg]	$\dot{\beta}_{\max}$ [deg/s]	$m_{\beta_{\max}}$ [Nm]
Actuator	0.56	65	15	40	Steady aero-m_β at $\beta = \beta_{\max}$
Sensors	1.0	190			

Table 1: Actuator and sensors parameters

accelerometer parameters are mostly dictated by the assumption of a second order anti-aliasing filter for the digital implementation, whose bandwidth is significantly below the one of the related sensor. Instead, plausible values for the actuators have been derived from the experimental data of [45], albeit with a bandwidth scaled down to 65 [rad/s], from 165, to take into account both a more easily achievable value and a more challenging controller design. The values of the actuator compliances have been found to be not critical over a sensible range of values and eventually set as reported in Table 2.

The design of the controllers could have been carried out either interactively or through a numerical op-

	NACA 64A010	BACT	Goland wing
k_β [Nm]	$7 \cdot 10^4$	$1.6 \cdot 10^4$	10^5

Table 2: Actuator compliances adopted for the three test cases.

timization which, because of the relatively low system order and smooth dependence on a small number of parameters, could have been based on an efficient gradient free optimizer, e.g. [46]. Eventually, the former option has been preferred. In fact, it requires no further coding and can be easily guided by following a simple heuristic procedure, based on the previously hinted physical understanding of the design parameters. The filter parameter μ is typically chosen in relation to the maximum frequency of the open loop system response, estimated by Fourier transforming a few time histories. Then, after verifying that a tentative $c_s = 1$ can be a suitable choice, γ_{Con} is computed accordingly to Eq. 38, followed by a few analyses carried out by maintaining $\lambda = 1$ while determining appropriately the values of c_s and γ_{Con} leading to a reasonable maximum control effort, eventually increasing λ until a desired settling time is achieved. On the other hand the observer demonstrated to work rather well with $\mathbf{Q} = \mathbf{I}$, $\mathbf{R} = 0.1\,\mathbf{I}$ and $\mathbf{Q}_s = 10\mathbf{I}$, along with a first guess of 0.1 for γ_{Obs}, followed by an open loop observer tuning, driven by the satisfaction of Eq. 48, until a fairly small estimation error is obtained. Furthermore $\mathrm{b}_d = 2$ and $\sigma = 2$ proved sufficient to achieve an adequate level of robustness and remained a common choice for all the following tests. Moreover, to assure the system adaptivity and stability over a wide range of operating conditions, the controller parameters are tuned considering various flight speed, at least 25 % greater than the open loop linearized flutter speed, combined with different type of simulations, such as the response to large initial conditions, to input pulses, eventually evaluating the controller adaption speed when its compensator is switched off-on during a simulation. Because of the simplified structure assumed for the observed ROM aerodynamic state, also an extensive set of verifications has been carried out by markedly biasing and randomly disturbing high fidelity generalized forces applied to the structure, so to simulate significantly different forces with respect to those used for tuning the control system. The results obtained were quite satisfactory, without any instability, contained control activity, with no significant saturation, except for the speed of the actuators. A sample result related to the following typical section, for $\mathbf{f}_a = \mathbf{f}_{a_{\mathrm{bias}}} + \mathbf{f}_{a_{\mathrm{nom}}}(\mathbf{1} + 4\,\mathbf{r}(t))$, is shown in Figure 3. The related terms are: the bias term, $\mathbf{f}_{a_{\mathrm{bias}}}$, set at the steady aeroelastic solution for $\theta = 5\,[\mathrm{deg}]$, $\mathbf{f}_{a_{\mathrm{nom}}}$ the nominal force provided by AeroFoam, $\mathbf{r}(t)$ a random normal time variation with a unit standard deviation. As it can be noticed, the aerodynamic uncertainties introduce a persistent disturbance in closed loop, deteriorating the convergence to the target dynamics. However, such a convergence is eventually recovered during the simulations, verifying the capability of the control system to withstand large model uncertainties. All the tuned designs and verifications have been determined by using an explicit Runge-Kutta integrator with adaptive step control, providing a precision adequate to allow avoiding an exact matching of saturation/desaturation time instants. Moreover a realistic digital implementation of the proposed controller has been taken into account. Through some preliminary continuous designs, it has been possible to verify that the sampled behavior of the continuous sliding observer and I&I compensator could be adequately matched at a frequency of 200 [Hz], the

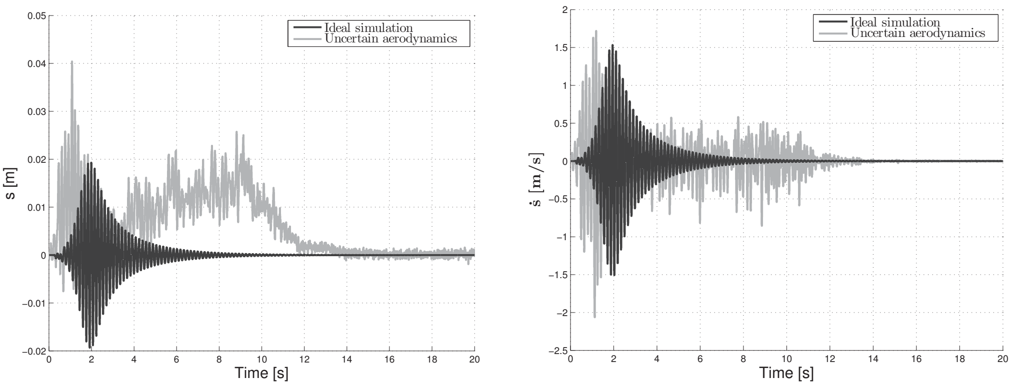

(a) s variable.

(b) $\dot{s}$ variable.

Figure 3: Effect of an uncertain aerodynamic model on the closed loop dynamics.

related discretization being based on a fix step Runge-Kutta-Heun integration scheme. To correctly simulate such a digitalization there is the need to care for the processing delay (input-calculation-output), associated to the chosen data acquisition system and control computer. Among the many carried out, Figure 4 shows a sample of the simulations comparing the controlled responses of the continuous and digitalized observer, at 200 [Hz] with a 60% (3 ms) processing delay. However, despite the many successful verifications obtained

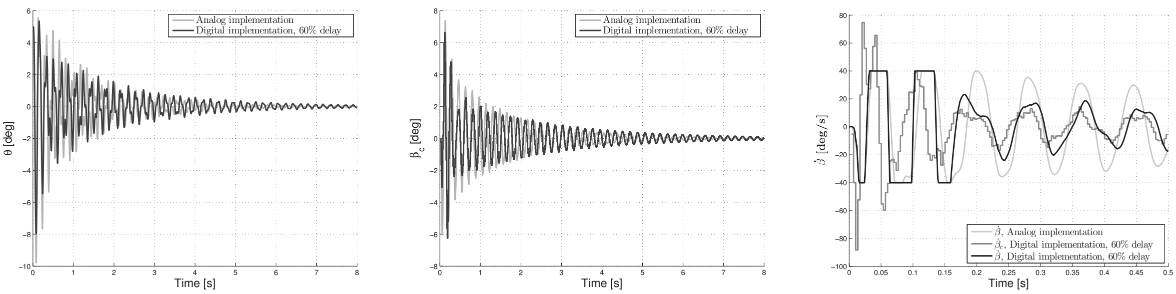

(a) Pitch response.

(b) Control surface deflection

(c) Control speed, with saturations.

Figure 4: Comparison of a continuous and digital controller implementation.

with the mentioned implementation parameters, all the following simulations will be based on the same 200 [Hz] sampling rate mated to a somewhat more conservative 30% (1.5 ms) processing delay.

In concluding this illustration of the features common to all the following test cases, it should be remarked that, for each of them, a vast set of simulations has been carried out against: varied ROM and finely discretized aerodynamic models, system disturbances and measurement noise, a $\pm 20\%$ change of most of the structural parameters. Nevertheless, for sake of brevity, only samples of the related results will be presented, trying to blend them in a way providing as a complete as possible picture of some interesting findings of this work.

V.A. NACA 64A010 typical wing section

This example has been chosen for two main reasons: it shows the ability of an I&I controller to stabilise the response of a significantly nonlinear system and demonstrates the importance of a correct modeling in the design phase.

It is related to a plunging and pitching typical section, featuring a NACA 64A010 airfoil, with a trailing edge flap, at sea level and $M_\infty = 0.8$ [47, 48], whose structural data are found in the Appendix. It is a kind of benchmark characterized by a significantly complex unsteady nonlinear aerodynamic behavior [47], producing an ample limit cycle having a frequency in excess of 10 [Hz], which cannot be matched by an overly simplified aerodynamic approximation.

For such a reason a reference high fidelity AeroFoam-Euler approximation of 12000 two dimensional cells, i.e. 48000 unknowns, will be used as the base for its validation. Moreover, because of its relatively high frequency limit cycle, it has not been possible to design a well working controller with an actuator bandwidth below 80 [rad/s]. After remarking that the servo-elastic subsystem will add just 12 states (6-structural, 2-actuator and 4-sensors), it should be clear that the overall system size is dominated by a huge number of aerodynamic states, which is unsuitable for the design of any active controller.

There is then the need to resort to a CTRNN based ROM, so the previously presented training procedure has been adopted, with $k_{\max} = 1$.

It converged to an acceptable ROM with only four aerodynamic states, see Figures 5a and 5b. Even-

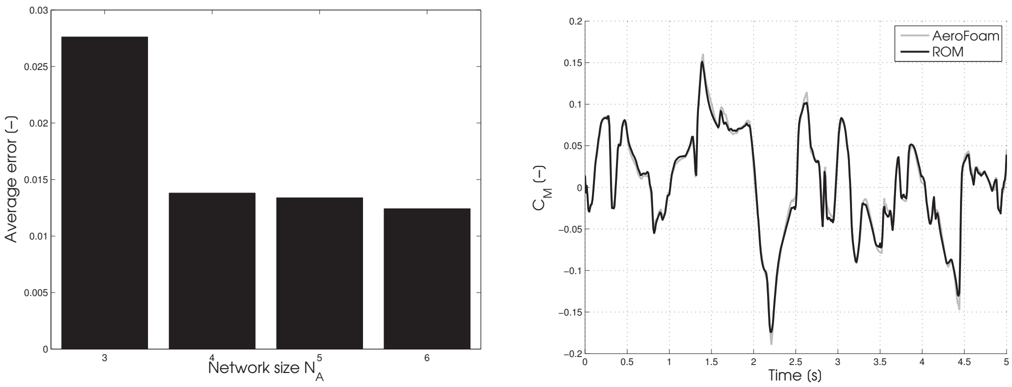

(a) Convergence analysis. (b) Aerodynamic moment coefficient.

Figure 5: Sample results of a neural network training.

tually, the resulting nonlinear aeroservoelastic model has sixteeen states and develops a limit cycle beyond a numerically estimated linearized flutter velocity $V_{\mathrm{F,OL}} = 193$ [m/s]. Figure 6 compares some trends of the ROM limit cycle parameters against their high fidelity counterparts. From such a comparison it is possible to infer a good amplitude match mated to somewhat differing frequencies, a discrepancy which could be corrected by using a larger order ROM. Nevertheless, in view of verifying the robustness of the to be designed I&I controller, such a imprecise low order ROM has been kept as it is.

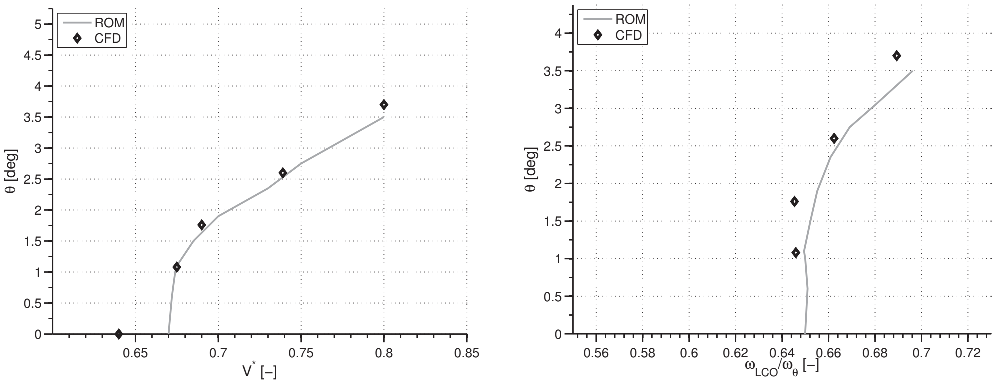

(a) Pitch amplitude vs. Velocity. (b) Pitch amplitude vs. Frequency.

Figure 6: ROM vs. high fidelity CFD for pitch amplitudes trends.

To achieve good adaptive performances against pulse perturbations applied through the flap, different flight speeds, up to 25% of $V_{\mathrm{F,OL}}$, are taken into account to tune the controller parameters. The target performance, Eq. 14, is the (linearized) vertical displacement at the leading edge of the typical section, so that, being $\mathbf{q} = [h \quad \theta \quad \beta \quad x_{\mathrm{act}} \quad x_{\mathrm{sens}_1} \quad x_{\mathrm{sens}_2}]^{\mathrm{T}}$ we have $\mathbf{H}_q = [1 \quad l_{\mathrm{LE}} \quad 0 \quad 0 \quad 0 \quad 0]$, where l_{LE} is the distance between the elastic center of the airfoil and its leading edge.

Carrying out the design with the interactive procedure previously described the control parameters of Table 3 are obtained: Using both the design ROM and high fidelity CFD, it is possible to show a few

γ_{Obs}	λ	c_s	μ	γ_{Con}	$2c_s\gamma_{\mathrm{Con}}$
0.5	50	30	750	0.04	$2.4 > \mathrm{b}_d$

Table 3: Controller parameters: typical section.

simulations illustrating the effectiveness of the obtained controller, implemented through its sixteen states sliding observer. At first, Figure 7 depicts a sample response of the controlled typical section to an input pulse applied at the design point. A significant random disturbance, having a maximum amplitude of 1.5 [deg], has been applied to the control surface, so showing the controller insensitivity to disturbances. Then a few high fidelity responses at the off-design condition of $V_\infty = 255$ [m/s] are presented in Figure 8, where the controller is switched on after $t = 4$ [s], when the limit cycle is fully developed. Spillover effects over the larger aerodynamic model have not been found in any of the verifications carried out. Some samples of the flow field during the limit cycle suppression are depicted in Figure 9, showing a significant shock oscillation amplitudes of the order of 23% of the chord. The controller appropriately cancels the large disturbance command applied by the control, eventually driving such a amplitude down to 2% of the chord. Nevertheless, despite the good results obtained, it can be useful to remark that the robustness of an I&I controller can result in being inadequate against excessively simplified design models, e.g. unmodeled sensor and actuator dynamics. For example, if we totally neglect those dynamics, a design at $V_\infty = 211$ [m/s] will

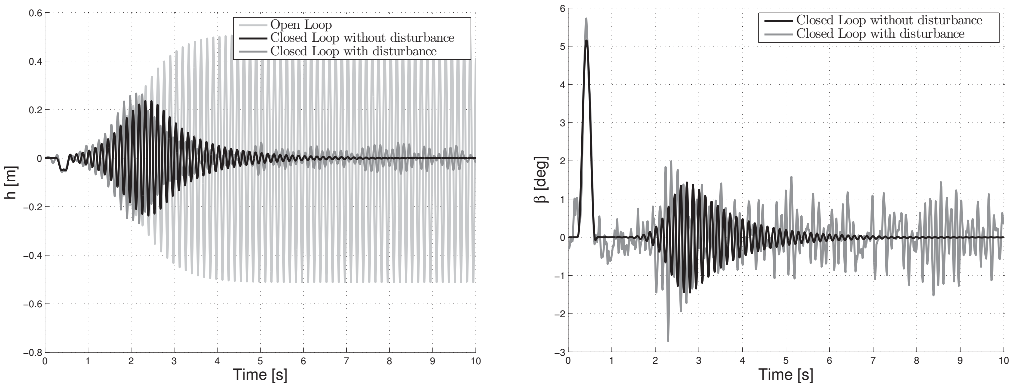

(a) Response to large initial condition on h. (b) Related control effort.

Figure 7: Input pulse response of the design model, $V_\infty = 211$ [m/s].

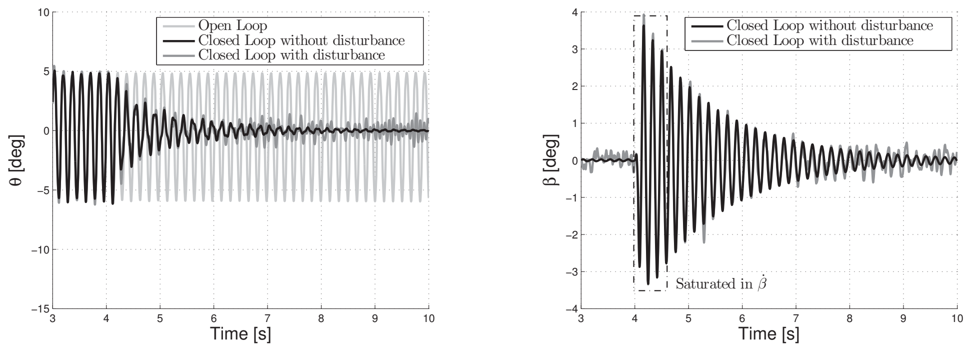

(a) Pitch response. (b) Related control effort.

Figure 8: High fidelity response to off-on control, $V_\infty = 255$ [m/s].

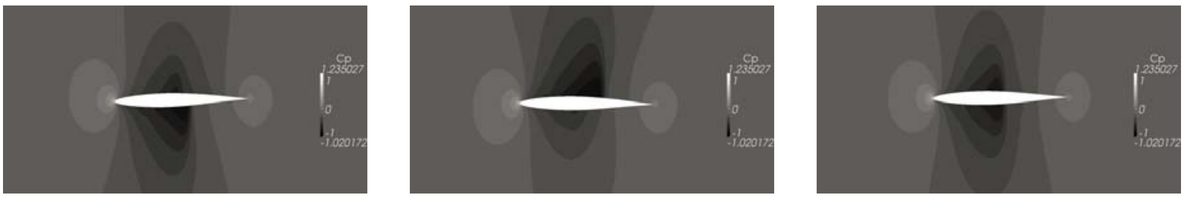

(a) Front position of the shock during the limit cycle. (b) Rear position of the shock during the limit cycle. (c) Stabilized position.

Figure 9: Various phases during the limit cycle oscillation suppression.

provide good performances with the parameters of Table 4, both for the reduced order and high fidelity CFD models, a sample of the surface rotation being depicted in Figure 10a.

Instead, by verifying the very same controller after accounting for its digital implementation and the very same actuator adopted in the previous design, we can see, Figure 10b, that it results in a rather violent instability. As witnessed by Figure 10c, something similar, albeit with a somewhat softer appearance, applies also after accounting for just the previously used sensor dynamics, even if its 25 [Hz] bandwidth is well in

γ_{Obs}	λ	c_s	μ	γ_{Con}	$2c_s\gamma_{\mathrm{Con}}$
0.5	50	30	125	0.1	$6 > \mathrm{b}_d$

Table 4: Controller parameters: ideal typical section, no sensor-actuator dynamics.

excess of the limit cycle frequency. Such outcomes clearly point out the need of taking into account any significant realization delay from the very inception of a design procedure.

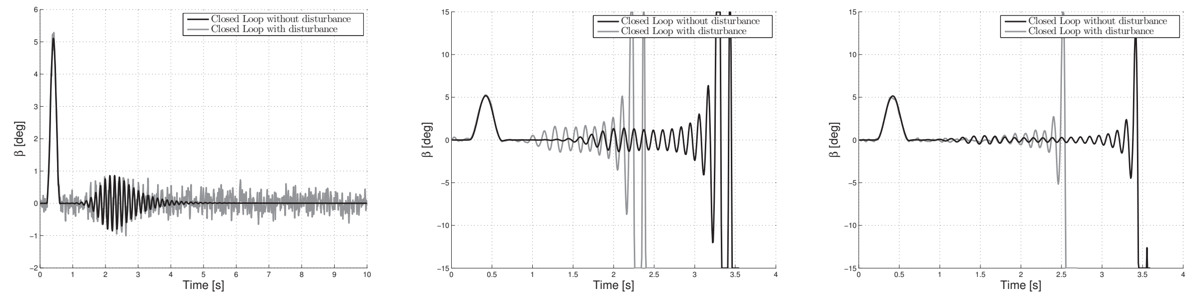

(a) Ideal control surface deflection.

(b) Ideal design response, after modeling the actuator.

(c) Ideal design response, after modeling the accelerometers.

Figure 10: Effects of omitting sensors and actuator dynamics in the design.

V.B. BACT wing model

As is has been already hinted at in the introduction, the Benchmark Active Controls Technology (BACT) project is part of NASA Langley Research Center's Benchmark Models Program for studying transonic aeroservoelastic phenomena. Therefore, it is a well known, easy to use, detailed and fully validated aeroservoelastic model [7,15,37], which has become an often referred benchmark application for verifying nonlinear aerodynamic analyses and active controls design methods. It is an elastically constrained rigid rectangular wing model, with NACA 0012 sections, equipped with a trailing-edge control surface and upper and lower-surface spoilers, which can be controlled independently through well performing hydraulic actuators. Its dynamic behavior is very similar to a classical typical section but, because of its low aspect ratio, it displays a not so simple three-dimensional transonic flow. However, it has been shown, e.g. [15], that the related nonlinear aerodynamic behavior is mild enough to produce slowly growing limit cycle oscillations, which can be verified only through high fidelity CFD validations [49]. Because of the above remark, the literature related to the design of active controllers for the BACT wing presents many instances of effective, experimentally validated, applications of linear design techniques [7,12,15,16].

In such a view the fully linear model, i.e. aerodynamics included, proposed in [37] will be used to design an I&I controller, to be verified against fully nonlinear CFD simulations afterward. Moreover, it should be remarked that in view of a quite small flutter reduced frequency, $k_F \approx 0.05$, such a model adopts also a highly simplified quasi-steady linearized unsteady aerodynamic approximation, i.e. as for Eq. 12 with

$\mathbf{f}_{a_{nl}}(\mathbf{x}_s) = \mathbf{0}$. Then, to ascertain a correct adoption of its data, the related design model, which has the same 12 state as the previous NACA64010 typical section, but without any added aerodynamic state, has been subjected to a few simple flutter calculations. A sample result, at Mach $M_\infty = 0.77$ in heavy gas R12 [37], a value that will be used also for all the following nonlinear verifications, shows a predicted flutter speed of $V_{\mathrm{F,OL}} = 108.58$ [m/s], only 1.3 % more than the corresponding test value. Once more, targeting the tip leading edge motion, the controller is designed to stabilise the wing up to a speed 35% higher than the original linear flutter point, against pulse perturbations applied through the aileron. Carrying out the usual interactive design procedure the control parameters of Table 5 are obtained. A sample of the results to an

γ_{Obs}	λ	c_s	μ	γ_{Con}	$2c_s\gamma_{\mathrm{Con}}$
0.01	50	30	30	0.4	$24 > \mathrm{b}_d$

Table 5: Controller parameters: BACT wing.

input pulse with an amplitude of 5 [deg] obtained during the design phase is shown in Figure 11. An efficient

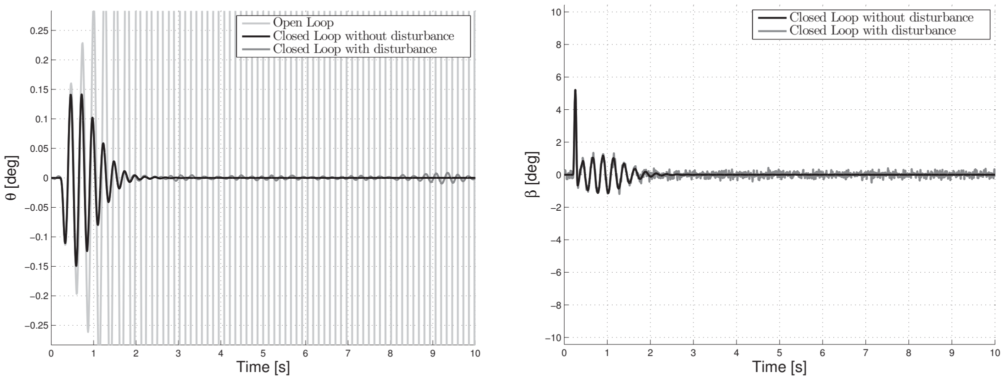

(a) Plunge output.

(b) Related control effort.

Figure 11: Response of the design model to a sizeable input pulse.

stabilisation with a limited control effort, even at a flight speed 20 % greater than the open-loop flutter speed, is worth being pointed out. It should be remarked also that, differently from other references [17, 19], a value $\gamma_{\mathrm{Con}} \sim 5$ has been verified to be a limiting stability bound, whereas higher values invariably produce an unstable controller.

The verification model consists of an FV discretization, whose fineness has been determined on the base of a steady-state convergence analysis, resulting in a mesh of 103040 cells (515200 aerodynamic state components). As already mentioned, the control robustness has been also verified against inertia and stiffness changes. A sample of such verifications, associated to a 20% increase of both bending and torsional stiffnesses at 135 [m/s], is shown in Figure 12, for an initial condition rather far away from the possible uncontrolled LCO and superimposing an initial strong aileron pulse to a random command. The adaption capability of the controller to appreciable changes of the nominal design should appear clearly, even in front of a significant

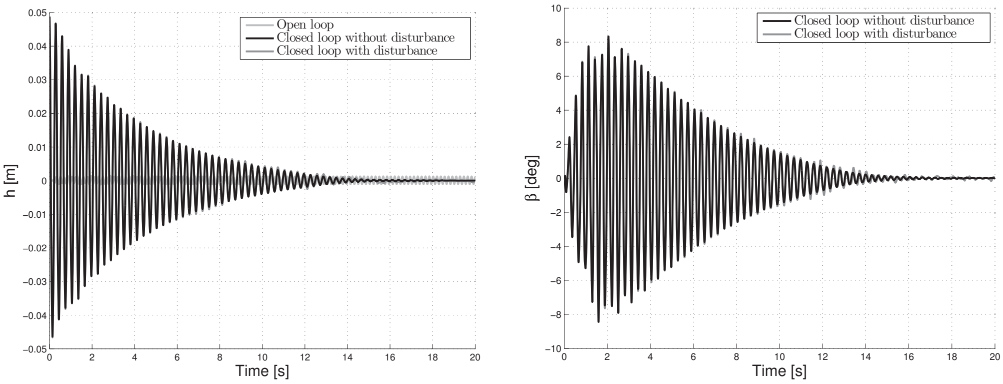

(a) Plunge output.

(b) Related control effort.

Figure 12: High fidelity response, BACT test case.

nonlinear aerodynamic behavior associated to a large shock motion, spanning 20 % of the wing chord during the initial part of the transient.

V.C. Goland wing

The Goland wing is a test case, found in the classical aeroelastic literature [23], which can exhibit both structural, wing and wing+store aerodynamic nonlinearities [24], of which only the one related to the aerodynamics of the clean wing will be considered here. The related geometry, aerodynamic, inertia and structural data, taken from [23], can be found in the Appendix. A proper modal basis, including the free rigid rotation of the here added trailing edge control surface, will be used to model the linear structure. The required 30 lower modes have been obtained through a 50 beams Finite Element (FE) discretization. In such a way the matrices $\mathbf{M}_s$, $\mathbf{C}_s$, and $\mathbf{K}_s$ will be diagonal, while, recalling that $\beta = \mathbf{T}_\beta \mathbf{q}_s$, $\mathbf{M}$, $\mathbf{C}$ and $\mathbf{K}$ will be coupled through the sensors and actuator dynamics, see Eqs. 7 and 8. It might also be worth pointing out that that each modal column of $\mathbf{T}_\beta$ is just the trivial difference between the rotation, θ, of the section at which the aileron is driven and the corresponding absolute modal rotation of the aileron itself.

This example considers a very simple aerodynamic model, i.e. a quasi-steady strip theory, linear in the design phase, nonlinear for the verifications. In fact, since a linear flutter analysis shows a bending-torsional flutter having a reduced frequency of only 0.01, similarly to the BACT wing, the adoption of such an approximation should be justifiable. Instead, in view of its somewhat low aspect ratio, a few, legitimate, doubts can be cast on the strip theory, which appears nonetheless to be used in other Goland based literature instances [24, 38]. That is likely because it is sufficiently adequate for a simpler qualitative demonstration of some nonlinear aerodynamic phenomena. In such a view, a span wise Schrenk's [50] correction is applied and the resulting model is exploited to verify how the proposed single input I&I controller can stabilize the nonlinear response of a test case closer to a real wing. So, calling x and y the chord and span wise running coordinates and s the wing span, we have:

$$
\begin{aligned}
C_L(y) &= 2\pi \left[\frac{1}{4s} + \frac{1}{2}\sqrt{1-(y/s)^2}\right](\alpha_{\text{eff}} + \tau\, W(y)\, \beta) \\
C_M(y) &= 2\pi\,(x_{\text{CA}} - x_{\text{EA}}) \left[\frac{1}{4s} + \frac{1}{2}\sqrt{1-(y/s)^2}\right](\alpha_{\text{eff}} + \tau\, W(y)\, \beta) \\
C_{M_h}(y) &= C_{M_h,\alpha}\alpha + C_{M_h,\beta}\beta \qquad\qquad W(y) = 1 \text{ for } y_a^{\text{start}} \le y \le y_a^{\text{end}},\ 0 \text{ elsewhere}
\end{aligned}
\tag{49}
$$

the coefficients $C_{L,\beta} = 1.25\,[1/\text{rad}]$ and $C_{M,\beta} = -1.85\,[1/\text{rad}]$, are estimated from thin airfoil theory, as well as $\tau = 0.33$, which is nonetheless decreased to 0.23 to penalize the 3D aileron efficiency. The angle of attack is defined as $\alpha(y) = \theta(y) + \dfrac{\dot{h}(y)}{V_\infty} + d_{3/4}\dot{\theta}$, being θ the wing torsional rotation, h the vertical displacement of the elastic axis, positive downward and $d_{3/4}$ the well known backward distance of the 3/4 chord point from the elastic axis.

In the verification stage an aerodynamic nonlinearity is taken into account by simply replacing α with the experimentally tuned $\alpha_{\text{eff}} = \alpha - 10.26\,\alpha^3$, valid for α up to $\pm 11\,[\text{deg}]$ [38].

Using the above approximation to calculate the generalized modal aerodynamic forces, the resulting linear terms will provide the matrices $\mathbf{C}_a$ and $\mathbf{K}_a$, with $\mathbf{M}_a = \mathbf{0}$, while the quadratic and cubic terms will be gathered in $\mathbf{f}_{a_{\text{nl}}}$.

Exploiting the previously presented modeling elements the design of the control parameters will proceed with 5 normal modes, including the rigid relative aileron rotation, for a total of 16 states (10-structure, 4-sensors, 2-actuator). Then the verification phase will be carried out on a refined model including many more modes and the above non linear correction of the angle of attack. Such an approach is similar to the one taken for the BACT wing, with the exception that the verification phase will not be based on high fidelity CFD simulations. In fact the aim of this example is directed to verifying the application of an I&I design to a servo-structural system a bit closer to a somewhat more realistic system. Because of such an assumption a more complex and complete modelling tool will likely not affect significantly the whole ROM based design and its high fidelity verifications.

A preliminary flutter analysis has been carried out for determining the stability of the aeroservoelastic system. The estimated flutter speed was found to be $V_{\text{F,OL}} = 38\,[\text{m/s}]$.

So, once more, the target performance $\tilde{y}$ is chosen to be the usual vertical displacement at the leading edge of the wing tip, thus synthesizing bending and torsion effects into a single variable. The needed single line target matrix $\mathbf{H}_q$ can be determined after calling: $\mathbf{q}_m$ the modes amplitudes vector, $\mathbf{T}_{h_{\text{tip}}}$ the modes displacements at tip leading edge and defining $\mathbf{q} = [\mathbf{q}_m^{\text{T}} \quad x_{\text{act}} \quad x_{\text{sens}_1} \quad x_{\text{sens}_2}]^{\text{T}}$, so that we have $\mathbf{H}_q = \begin{bmatrix}\mathbf{T}_{h_{\text{tip}}} & 0 & 0 & 0\end{bmatrix}$.

The controller can then be designed to stabilize the wing up to a speed 40% higher than the original linear flutter speed, in front of pulse perturbations introduced by the aileron. So, carrying out the interactive design procedure, the control parameters of Table 5 are obtained. A sample of an almost converged design iteration

γ_{Obs}	λ	c_s	μ	γ_{Con}	$2c_s\gamma_{\mathrm{Con}}$
0.1	20	10	120	0.2	$4 > \mathrm{b}_d$

Table 6: Controller parameters: Goland wing.

is shown in Figure 13 for the application of a 5 [deg] aileron deflection for 0.2 [s]. The controller robustness

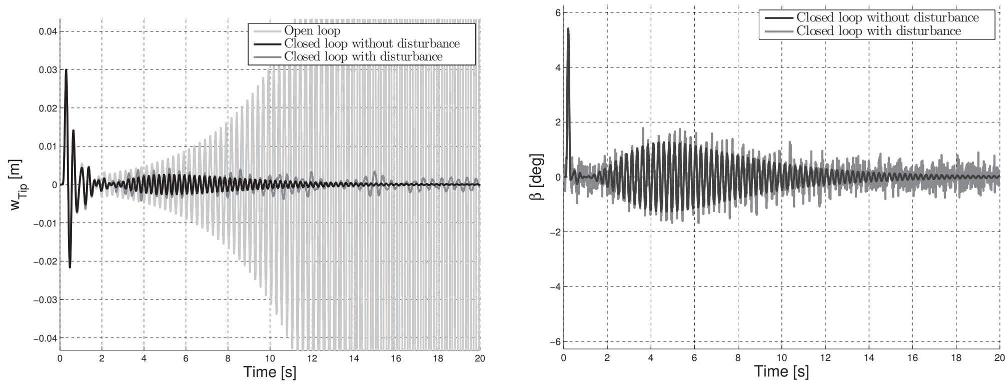

(a) Vertical displacement at the wing tip.

(b) Related aileron deflection.

Figure 13: Design model response to a sizeable aileron pulse.

verification against modal spillover and model uncertainties will be based on model with 30 vibration modes, i.e. 60 structural states, 6 sensor-actuator states and the nonlinear aerodynamic model. Figure 14 shows a sample of the obtained results for the response to a large initial condition with a random distrurbance of 2 [deg] commanded by the control surface, at a flow speed 30 % in excess of the open-loop flutter speed. To prove the fast adaptivity of the proposed controller, the control action is switched on after the limit cycle is fully developed. It should come to little surprise that for such a speed and disturbances the initial control

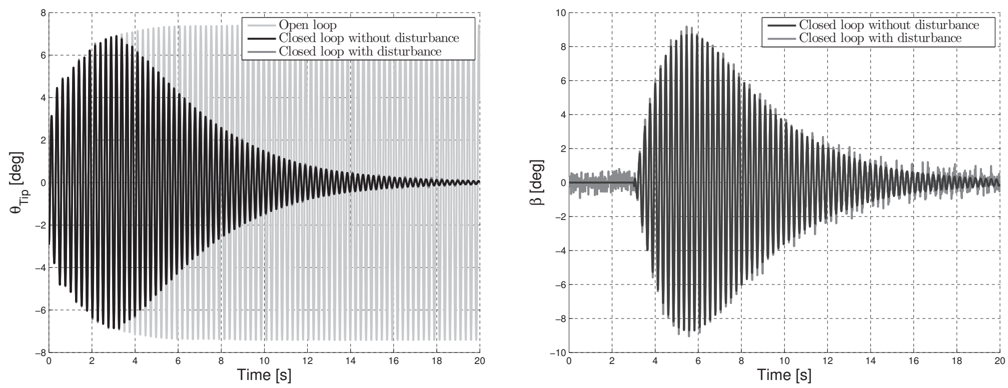

(a) Wing tip rotation.

(b) Related aileron deflection.

Figure 14: Quasi-steady nonlinear aerodynamic verification to off-on control.

effort is quite significant. Nevertheless it can be verified that related response evidences again the robustness of the adaptive I&I controller.

As a further robustness demonstration, a series of detailed verifications have been carried out on a modified models with weakened bending and torsional stiffnesses. It is then possible to track the trend of the maximum control effort against the related stiffness changes at a fixed flight speed. The test velocity is 35% higher than $V_{\mathrm{F,OL}}$ and the applied disturbance is an aileron pulse having an amplitude of 5 [deg] and duration of 0.2 [s]. The obtained trends are shown in Figure 15.

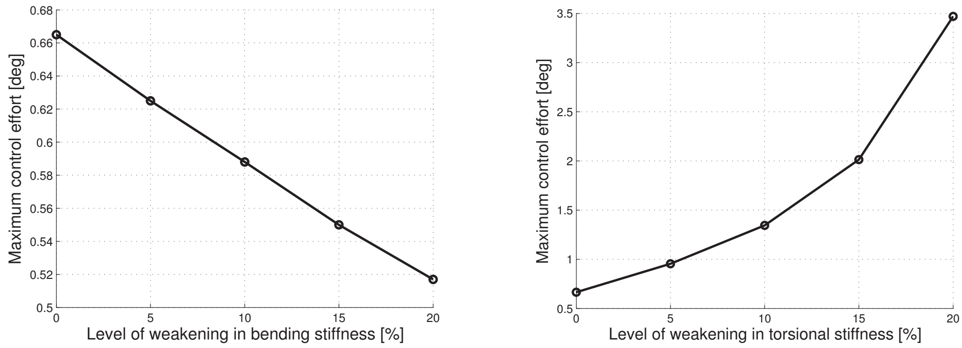

(a) Maximum control efforts vs. bending stiffness. (b) Maximum control efforts vs. torsional stiffness.

Figure 15: Results of a robustness verification on the Goland wing.

It should be noticed that the control effort is much more affected by the torsional stiffness changes, whereas a reduction of the bending stiffness results in a decreased maximum control effort. This is likely due to the effect that a decreasing bending stiffness has on the flutter behavior of the wing. In fact, reducing the frequency of the first bending mode results in a slight postponement of the bending-torsion flutter onset.

VI. Concluding Remarks

The paper has presented an adaptive approach for the active suppression of a possible nonlinear flutter through a full state Immersion and Invariance (I&I) controller, coupled to a sliding mode observer. The performance of such a controller has been verified on three typical aeroelastic test cases: a typical wing section, the BACT wing benchmark model and the Goland wing, with mathematical models representing their aerodynamic subsystem at different levels of fidelity, ranging from quasi-steady nonlinear approximations, to full and ROM based CFD formulations. It should be remarked that one of the tests, the Goland wing, provides a simple, yet not trivial, application involving a deformable beam model, which is somewhat closer to possible more realistic applications. Because of the small number of design parameters, the adopted interactive design procedure, based on well reasoned and physically understood simulations, has been verified to be an adequate tool. In fact the resulting adaptive controllers provided fairly robust stabilisation properties against differing flow conditions, sizeable system disturbances, model order and parameters variations. Moreover the importance of embodying appropriate formulations of the dynamics of sensors and actuators has been verified, whereas neglecting them could lead to a loss of robustness, mated to a difficult implementation. It is believed that to fully verify the strength and weaknesses of a non linear adaptive I&I controller there remains the need of focusing on more complex and realistic applications, e.g. multi input and deformable free flying aircraft, integrating true design specifications related to stability and response performances.

A. Appendix: Models Data

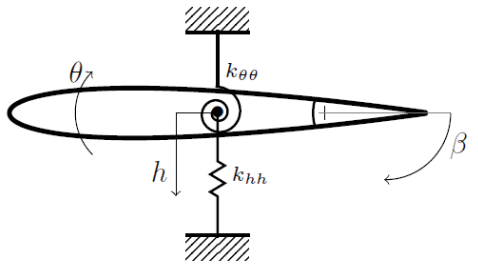

Figure 16: Typical section degrees of freedom.

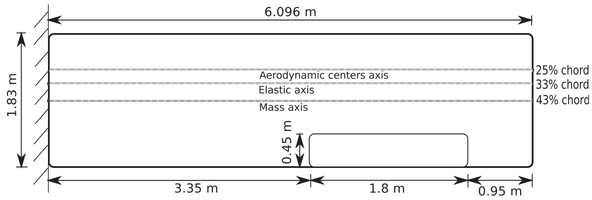

Figure 17: Goland wing geometry, $d_{3/4} = 0.43\,[m]$.

$$\mathbf{q}_s = \begin{Bmatrix} h \\ \theta \\ \beta \end{Bmatrix} \quad \mathbf{M}_s = \begin{bmatrix} m & S_{h\theta} & S_{h\beta} \\ S_{h\theta} & J_{\theta\theta} & 0 \\ S_{h\beta} & 0 & J_{\beta\beta} \end{bmatrix} \quad \mathbf{C}_s = \begin{bmatrix} 2\xi_{hh} m\,\omega_{hh} & 0 & 0 \\ 0 & 0.002 J_{\theta\theta}\,\omega_{\theta\theta} & 0 \\ 0 & 0 & 0 \end{bmatrix} \quad \mathbf{K}_s = \begin{bmatrix} m\omega_{hh}^2 & 0 & 0 \\ 0 & J_{\theta\theta}\omega_{\theta\theta}^2 & 0 \\ 0 & 0 & 0 \end{bmatrix}$$

Typical section: mass, damping and stiffness matrices; $\mathbf{q}_s = [\text{plunge, pitch, trailing edge control}]^{\mathrm{T}}$.

	m	$J_{\theta\theta}$	$J_{\beta\beta}$	$S_{h\theta}$	$S_{h\beta}$	ω_{hh}	$\omega_{\theta\theta}$	ξ_{hh}	c	b	x_h
	[kg]	[kgm^2]	[kgm^2]	[kgm]	[kgm^2]	[rad/s]	[rad/s]	[-]	[m]	[m]	$\%c$
NACA64010	29.45	5.52	1.50	3.68	0.1178	40.5	81.0	0.001	1.0	0.5	75
BACT	88.7	3.80	1.00	0.0631	0.0128	21.01	32.72	0.0014	0.4048	0.8096	75

Table 7: NACA64010 typical section and BACT wing data.

m	$J_{\theta\theta}$	$J_{\beta\beta}$	$S_{h\theta}$	$S_{h\beta}$	modal damping	bending stiffness EJ	torsional stiffness GJ
[kg/m]	[kgm]	[kgm]	[kg]	[kgm]	[-]	[Nm^2]	[Nm^2]
35.72	8.64	0.4	6.52	0.05	0.005	994506.6	100714.9

Table 8: Goland wing uniform inertias per unit length, modal damping and uniform bending and torsional stiffnesses.

References

[1] Jacklin, S. A., "Closing the Certification Gaps in Adaptive Flight Control Software," Tech. rep., NASA Ames Research Center, 2008.

[2] Schumann, J., Gupta, P., and Nelson, S., "On Verification and Validation of Neural Network Based Controllers," Tech. rep., NASA, 2003.

[3] Mukhopadhyay, V., "Historical Perspective on Analysis and Control of Aeroelastic Responses," *Journal of Guidance, Control and Dynamics*, Vol. 26, 2003, pp. 673–684.

[4] Friedmann, P., Guillot, D., and Presente, E., "Adaptive Control of Aeroelastic Instabilities in Transonic Flow and Its Scaling," *Journal of Guidance, Control and Dynamics*, Vol. 20, 1997, pp. 1190–1199.

[5] Becker, K. and Vassberg, J., "Numerical Aerodynamics in Transport Aircraft Design," *Notes on Numerical Fluid Mechanics*, Vol. 100, 2009, pp. 209–220.

[6] Chen, G., Sun, J., and Li, Y., "Adaptive Reduced-Order-Model-Based Control-Law Design for Active Flutter Suppression," *Journal of Aircraft*, Vol. 49, 2012, pp. 973–980.

[7] Waszak, M. R., "Robust Multivariable Flutter Suppression for the Benchmark Active Control Technology (BACT) Wind-Tunnel Model," *11th Symposium on Structural Dynamics and Control, Blacksburg, VA*, 1997.

[8] Rubillo, C. and Marzocca, P., "Active Aeroelastic Control of Lifting Surfaces Via Jet Reaction Limiter Control," *International Journal of Bifurcation and Chaos*, Vol. 16, 2006, pp. 2559–2574.

[9] Wise, K. A., Lavretsky, E., and Hovkimyan, N., "Adaptive Control of Flight: Theory, Applications, and Open Problems," *Proceedings of the 2006 American Control Conference*, 2006.

[10] Lee, K. W. and Singh, S. N., "Immersion- and Invariance-Based Adaptive Control of a Nonlinear Aeroelastic System," *Journal of Guidance, Control and Dynamics*, Vol. 32, 2009, pp. 1100–1110.

[11] Andrighettoni, M. and Mantegazza, P., "Multi-Input/Multi-Output Adaptive Active Flutter Suppression for a Wing Model," *Journal of Aircraft*, Vol. 35, 1998, pp. 462–469.

[12] Scott, R. and Pado, L., "Active Control of Wind Tunnel Model Aeroelastic Response Using Neural Networks," *Journal of Guidance, Control and Dynamics*, Vol. 23, 2001, pp. 1100–1108.

[13] Bernelli-Zazzera, F., Mantegazza, P., Mazzoni, G., and Rendina, M., "Active Flutter Suppression Using Recurrent Neural Networks," *Journal of Guidance, Control and Dynamics*, Vol. 23, 2000, pp. 1030–1037.

[14] Mattaboni, M., Quaranta, G., and Mantegazza, P., "Active flutter suppression for a three surface transport aircraft by recurrent neural networks," *48th AIAA/ASME/ASCE/AHS/ASC Structures, Structural Dynamics and Materials Conference, Honolulu, HI*, 2007.

[15] Mukhopadhyay, V., "Transonic Flutter Suppression Control Law Design and Wind-Tunnel Test Results," *Journal Of Guidance, Control and Dynamics*, Vol. 23, 2000, pp. 930–937.

[16] Kelkar, A. G. and Joshi, S. M., "Passivity-Based Robust Control with Application to Benchmark Active Controls Technology Wing," *Journal of Guidance, Control and Dynamics*, Vol. 23, 2000, pp. 938–947.

[17] Astolfi, A., Karagiannis, D., and Ortega, R., *Nonlinear and Adaptive Control with Applications*, Springer, 2008.

[18] Astolfi, A., Karagiannis, D., and Ortega, R., "Toward Applied Nonlinear Adaptive Control," *Annual Reviews in Control*, Vol. 32, 2008, pp. 136–148.

[19] Seo, D. and Akella, M. R., "High Performance Spacecraft Attitude-Tracking Control Through Attracting Manifold Design," *Journal of Guidance, Control and Dynamics*, Vol. 31, 2008, pp. 884–891.

[20] Seo, D. and Akella, M. R., "Non-Certainty Equivalent Adaptive Control for Robot Manipulator Systems," *System and Control Letters*, Vol. 58, 2009, pp. 304–308.

[21] Lee, K. and Singh, S. N., "Non-Certainty-Equivalent Adaptive Control of a Nonlinear Aeroelastic System," *International Journal of Electronics and Telecommunications*, Vol. 56, 2010, pp. 463–471.

[22] Lee, W. L. and Singh, S. N., "Multi-Input Noncertainty-Equivalent Adaptive Control of an Aeroelastic System," *Journal of Guidance, Control and Dynamics*, Vol. 33, 2010, pp. 1451–1460.

[23] Bisplinghoff, R. L., Ashley, H., and Halfman, R. L., *Aeroelasticity*, Dover, 1955.

[24] Kim, K. and Strganac, T., "Aeroelastic Studies of a Cantilever Wing with Structural and Aerodynamic Nonlinearities," *43rd AIAA/ASME/ASCE/AHS/ASC Structures, Structural Dynamics, and Materials Conference, Denver, CO*, 2002.

[25] Romanelli, G., Serioli, E., and Mantegazza, P., "A "Free" Approach to Computational Aeroelasticity," *48th AIAA Aerospace Sciences Meeting and Exhibit, Orlando, FL*, 2010.

[26] Romanelli, G., Castellani, M., Mantegazza, P., and Ricci, S., "Coupled CSD/CFD non-linear aeroelastic trim of free-flying flexible aircraft," *53rd AIAA/ASME/ASCE/AHS/ASC Structures, Structural Dynamics and Materials Conference, Honolulu, HI*, 2012.

[27] Ripepi, M. and Mantegazza, P., "Improved Matrix Fraction Approximation of Aerodynamic Transfer Matrices," *AIAA Journal*, Vol. 51, 2013, pp. 1156–1173.

[28] Hall, K., Thomas, J., and Dowell, E., "Proper Orthogonal Decomposition Technique for Transonic Unsteady Aerodynamic Flows," *AIAA Journal*, Vol. 38, 2000, pp. 1853–1862.

[29] Lucia, D. J., Beran, P. S., and Silva, W. A., "Reduced-order modeling: new approaches for computational physics," *Progress in Aerospace Sciences*, Vol. 40, 2004, pp. 51–117.

[30] Chen, G., Li, Y., and Yan, G., "Nonlinear POD Reduced Order Model for Limit Cycle Oscillation Prediction," *Science China Physics, Mechanics and Astronomy*, Vol. 53, Issue 7, 2010, pp. 1325–1332.

[31] Silva, W., "Identification of Nonlinear Aeroelastic Systems Based on the Volterra Theory: Progress and Opportunities," *Nonlinear Dynamics*, Vol. 39, 2005, pp. 25–62.

[32] Balajewicz, M. and Dowell, E., "Reduced-Order Modeling of Flutter and Limit-Cycle Oscillations Using the Sparse Volterra Series," *Journal Of Aircraft*, Vol. 49, 2012, pp. 1803–1812.

[33] Glaz, B., Li, L., and Friedmann, P. P., "Reduced-Order Nonlinear Unsteady Aerodynamic Modeling Using a Surrogate-Based Recurrence Framework," *AIAA Journal*, Vol. 48, 2010, pp. 2418–2429.

[34] Mannarino, A. and Mantegazza, P., "Nonlinear Aeroelastic Reduced Order Modeling By Recurrent Neural Networks," *Journal of Fluids and Structures*, 2014, to be published.

[35] Etkin, B., "Aerodynamic Transfer Functions: An Improvement on Stability Derivatives for Unsteady Flight," Tech. rep., University of Toronto, 1956.

[36] Pasinetti, G. and Mantegazza, P., "Single Finite States Modeling of Aerodynamic Forces Related to Structural Motions and Gusts," *AIAA Journal*, Vol. 37, 1999, pp. 604–612.

[37] Waszak, M. R., "Modeling the Benchmark Active Control Technology Wind-Tunnel Model for Active Control Design Applications," Tech. rep., NASA, 1998.

[38] Kim, K. U. and Strganac, T. W., "Nonlinear Responses of a Cantilever Wing with an External Store," *44th AIAA/ASME/ASCE/AHS Structures, Structural Dynamics, and Materials Conference, Norfolk, VA*, 2003.

[39] Slotine, J.-J. E. and Li, W., *Applied Nonlinear Control*, Prentice Hall, 1991.

[40] Ioannou, P. A. and Kokotovic, P. V., "Instability Analysis and Improvement of Robustness of Adaptive Control," *Automatica*, Vol. 20, 1984, pp. 583–594.

[41] Ioannou, P. and Baldi, S., *Robust Adaptive Control. The Control Handbook, Chapter 35*, CRC Press, Second Edition, 2010.

[42] Ioannou, P. and Sun, J., *Robust Adaptive Control*, Dover Publications, 2012.

[43] Atassi, A. N. and Khalil, H. K., "A Separation Principle for the Stabilization of a Class of Nonlinear Systems," *IEEE Transactions on Automatic Control*, Vol. 44, 1999, pp. 1672–1687.

[44] Drakunov, S. and Utkin, V., "Sliding Mode Observers. Tutorial." *Proceeding of the 34th Conference on Decision&Control, New Orleans, LA*, 1995, pp. 3376–3378.

[45] Waszak, M. and Fung, J., "Parameter estimation and analysis of actuators for the BACT wind-tunnel model," *21th AIAA Atmospheric Flight Mechanics Conference, San Diego,CA*, 1996.

[46] Powell, M. J. D., "LINCOA, a derivative free Linearly Constrained Optimization Algorithm," *FORTRAN code available at <mat.uc.pt/~zhang>*, 2013.

[47] Thomas, J. P., Dowell, E. H., and Hall, K. C., "Nonlinear inviscid aerodynamic effects on transonic divergence, flutter, and limit-cycle oscillations," *AIAA Journal*, Vol. 40, 2002, pp. 638–646.

[48] Yao, W. and Liou, M., "Reduced-order modeling for flutter/LCO using recurrent artificial neural network," *12th AIAA Aviation Technology, Integration, and Operations (ATIO) Conference and 14th AIAA/ISSM, Indianapolis, IN*, 2012.

[49] Zhang, W., Wang, B., and Ye, Z., "High efficient numerical method for limit cycle flutter analysis based on nonlinear aerodynamic reduced-order-model," *51st AIAA, ASME, ASCE, AHS, ASC Structures, Structural Dynamics and Material Conference, Orlando, FL*, 2010.

[50] Schrenk, O., "A simple approximation method for obtaining the spanwise lift distribution," Tech. rep., Technical Memorandums NACA, 1940.